UNIVERSITY OF CALIFORNIA
RIVERSIDE

The Lyman Continuum Escape Fraction of Star Forming Galaxies at $z \sim 2 - 3$

A Dissertation submitted in partial satisfaction
of the requirements for the degree of

Doctor of Philosophy

in

Physics

by

Seyed Kaveh Vasei Zadeh Kashani

December 2018

Dissertation Committee:
Dr. Brian Siana, Chairperson
Dr. Bahram Mobasher
Dr. Naveen Reddy

The Dissertation of Seyed Kaveh Vasei Zadeh Kashani is approved:

_____

_____

_____

Committee Chairperson

University of California, Riverside

Acknowledgements

I am grateful to everyone who made this Ph.D. dissertation possible. A comprehensive list of people who played an essential role in the process is not feasible, however, a few people immediately come to mind.

My advisor, Brian Siana, provided me with a tremendous degree of freedom and many opportunities over the years. His expertise and supportiveness and easy to approach attitude allowed me to focus on research.

I thank my wife, Anahita, for supporting me through the very stressful final year of my dissertation research. I thank my son, Aubteen for providing me with extra motivation and brightening the final months of my research with his wonderful smile and contagious laugh. And my Parents, without their sacrifices I would not have been capable of pursuing an advanced degree abroad.

Additionally, I would like to thank my thesis committee: Prof. Naveen Reddy and Prof.Bahram Mobasher for their insightful comments and questions. In particular, I thank Prof.Reddy for all the discussions that I had with him and his valuable comments about different parts of my Ph.D. projects. In addition, I am very grateful to Prof. Mobasher for encouraging me to come to UCR and all his help when I had just started as an international student and supporting my family. I also thank Prof. Gabriela Canalizo for being in my qualifying exam committee and for her constant encouragement(food) throughout my research period.

I am so grateful of my fellow colleagues Anahita Alavi, William Freeman, Najmeh Emami, Louise Daniels, Tim Gburek and our new teammate Chris for their friendship and all the fun that we had during our group meetings. I also thank Hooshang Nayyeri, Shoubaneh Hemmati, Behnam Darvish, Ali Ahmad Khostovan and Omid Sameie for many interesting discussions and activities that we had during graduate school. I want

to thank Dr. Mario De Leo Winkler for all his endeavors for promoting outreach activities in our astronomy group and providing a joyful opportunity for graduate students including me to jointly work with him. A special thanks to the Physics department student affairs officer Dr. Derek Beving who was always very helpful whenever I had any question or I needed any paperwork.

The text of this dissertation, in part, is a reprint of the material as it appears in a journal article entitled *The Lyman Continuum Escape Fraction of the Cosmic Horseshoe: A Test of Indirect Estimates*, which appeared in volume 831 (page 38) of The Astrophysical Journal, November 1st, 2016.

ABSTRACT OF THE DISSERTATION

The Lyman Continuum Escape Fraction of Star Forming Galaxies at $z \sim 2-3$

by

Seyed Kaveh Vasei Zadeh Kashani

Doctor of Philosophy, Graduate Program Physics
University of California, Riverside, December 2018
Dr. Brian Siana, Chairperson

Star-forming galaxies are widely believed to be responsible for the reionization of the Universe and much of the ionizing background at z>3. Therefore, there has been much interest in quantifying the escape fraction of the Lyman continuum (LyC) radiation of the star-forming galaxies. Yet direct detection of LyC has proven to be exceptionally challenging. Despite numerous efforts only 8 galaxies at z<2 (all but one with escape fractions less than 0.04) and 4 galaxies at z>2 have been robustly confirmed as LyC leakers. To avoid these challenges many studies use indirect methods to infer the LyC escape fraction. We tested these indirect methods by attempting to detect escaping LyC with a 10-orbit Hubble near-UV (F275W) image that is just below the Lyman limit at the redshift of the Cosmic Horseshoe (a lensed galaxy at z=2.4). We concluded that the measured escape fraction is lower, by more than a factor of five, than the expected escape fraction based on the indirect methods. This emphasizes that indirect determinations should only be interpreted as upper-limits.

We also investigated the deepest near-UV Hubble images of the SSA22 field to detect LyC leakage from a large sample of candidate star-forming galaxies at z $\sim$ 3.1, whose redshift was obtained by deep Keck/LRIS spectroscopy and for which Keck narrow-band imaging was showing possible LyC leakage. The high spatial resolution of Hubble images is crucial to confirm our detections are clean from foreground contaminating galaxies, and also to ascertain the escape fraction of our final candidates. We identify four clean LyC emitting star-forming galaxies, which doubles the sample of confirmed LyC leakers found till now. The follow up investigation of these galaxies will significantly increase our knowledge of the LyC escape fraction and the mechanisms allowing for LyC escape.

Contents

List of Figures

List of Tables

Chapter 1

Introduction

Observations of high-redshift quasars and galaxies and the cosmic microwave background have revealed the reionization history of the universe, which is largely finished at z= 6 (e.g., Fan et al. 2006; Stark et al. 2011; Robertson et al. 2013; Schenker et al. 2014; Bian et al. 2015; Bouwens et al. 2015a; Planck Collaboration et al. 2016). Star-forming galaxies are expected to be responsible for the reionization of the intergalactic hydrogen at $z > 7$ (e.g., Robertson et al. 2015) and much of the ionizing background at $3 < z < 7$ (Becker and Bolton, 2013; Nestor et al., 2013; Becker et al., 2015). Several studies have determined that the number density of active galactic nuclei (AGNs) is not high enough to provide the required ionizing background (Inoue et al. 2006; Siana et al. 2008; Willott et al. 2010; Masters et al. 2012), although an identification of a numerous population of "faint" AGNs at $4 < z < 6.5$ (Giallongo et al. 2015) indicates that the contribution of AGNs to the cosmic reionization at early epochs may be more important than previously assumed (Glikman et al. 2011; Fontanot et al. 2012; Madau Haardt 2015; Khaire et al. 2016).

Whether or not stars reionized the inter-galactic medium (IGM) and provided the ionizing background for the next 1 - 2 Gyr thereafter, is largely contingent upon a few

uncertain parameters: the total star formation rate density, including the significant contribution from sources beyond our current detection limits; the intrinsic ionizing spectrum of the galaxies; the fraction of this ionizing radiation that escapes into the IGM; and the "clumping factor" of the hydrogen being ionized in the IGM at any epoch (and thus the recombination rate).

Many efforts, both theoretical and observational, are being made to determine the amount of undetected star formation (Alavi et al. 2014 ; Bouwens et al. 2015b, 2016; Livermore et al. 2017) and the clumping factor (Pawlik et al. 2009; Finlator et al. 2012). However, very little is understood about the "escape fraction", f_{esc}, of ionizing radiation. To contribute enough ionizing photons to reionization of the universe, it is required that the LyC escape fraction (fesc) be comparable to or larger than 0.2 at the epoch of the reionization (e.g., Ouchi et al. 2009; Robertson et al. 2013).

The majority of ionizing photons are emitted by massive O-stars which form in dense molecular clouds and In order for a significant fraction of ionizing radiation to escape into the IGM, lines of sight (LOSs) with low neutral hydrogen column density must be cleared out or the stars must migrate out of the gas. Either process must occur within the short lifetime ($\leq$10 Myr) of the type O stars that produce the ionizing radiation. Though it is not understood exactly how the stars can be exposed on such short timescales several mechanisms has been proposed. This include the effect of supernova (SN) feedback (e.g., Dove et al. 2000; Fujita et al. 2003; Ma et al. 2015), or could be due to interactions or merging with other galaxies (Gnedin et al. 2008), or runaway massive stars (e.g. Conroy and Kratter, 2012). Each of these mechanisms by which LyC photons can escape the host galaxy lead to a distinguished observational signatures based on the morphological distribution of the escaping LyC. Hence spatially resolved, directly detected LyC emitters can shed light on which of these processes are responsible for high escape fractions and, thus, the reionization of the universe.

If SN winds clear low column density sight lines, then the LyC primarily is concentrated on the regions with highest star formation surface density. But if the galaxy interactions or runaway stars are the main mechanism, then LyC emission will be less concentrated. Though, no matter what is the main mechanism behind the escaping LyC, the aim is to measure the average escape fraction and any dependencies it might have on galaxy properties or environment.

Direct observations of galaxies are only viable up to redshifts $z \sim 3.5$, beyond which the rest-frame LyC emission becomes unobservable due to the increasing IGM opacity (e.g. Madau 1995). A viable strategy implies the search for $z < 4$ LyC-leaking galaxies and use their characteristic properties to identify high-redshift analogs, whose LyC cannot be directly observed (e.g. Zackrisson et al. 2013; Schaerer et al. 2016). Hence in the past two decades, the search for Lyman continuum leakers has been extensively conducted by many surveys of star-forming galaxies at $z \leq 4$ (e.g., Leitherer et al. 1995; Steidel et al. 2001; Shapley et al. 2006; Siana et al. 2007, 2010, 2015; Grimes et al. 2007,2009; Cowie et al. 2009; Iwata et al. 2009; Bridge et al. 2010; Vanzella et al. 2010, 2012, 2015, 2016; Nestor et al. 2011,2013; Mostardi et al. 2013; Guaita et al. 2016; Grazian et al. 2016; Marchi et al. 2016).

Among thousands of inspected galaxies, after accounting for contamination of superimposed foreground sources, which becomes increasingly more important when moving towards higher redshifts and lower luminosities (Vanzella et al. 2010; Mostardi et al. 2015; Siana et al. 2015), only a handful of sources with Secure spectroscopically confirmed detections of the LyC from star-forming galaxies have been found in the local Universe. At low redshifts (z 0.3) Bergvall et al. 2006; Leitet et al. 2013; Borthakur et al. 2014; Izotov et al. 2016b,a and at high redshifts ($z \sim 2 - 3$) (de Barros et al. 2016; Vanzella et al. 2016; Shapley et al. 2016, Bian et al.2017).

Many uncertainties remain in understanding ionizing photon escape constraints

from various studies. Foremost among these is the possibility of foreground contamination of the z $\sim$ 3 LyC detected galaxies. In some cases, it is possible that a faint star-forming galaxy lies along the LOS to the target galaxy, but at significantly lower redshift. In this case a candidate detection in the rest-frame LyC of the background galaxy could simply be non-ionizing emission from the foreground galaxy.

Some studies have used deep U-band number counts (which probes below the Lyman limit above z $\sim$ 3) to determine the probability of foreground contamination at z $\sim$ 3 (Siana et al. 2007,2015; Vanzella et al. 2010b; Nestor et al. 2011; Mostardi et al. 2013) and find that a significant fraction of LyC detections are in fact attributed to foreground contamination. This contamination fraction is a strong function of the depth of the LyC images (since the number density of foreground objects rises steeply at fainter magnitudes; e.g., Alavi et al. 2014,2016), as well as the FWHM of the point-spread function (PSF) (as the PSF widens, contaminants at larger impact parameters cannot be recognized).However, the foreground object may lack strong emission lines or the lines may be shifted out of the wavelength range covered by the spectrum. A high signal-to-noise ratio (S/N) detection of the continuum of the background galaxy is required to identify foreground absorption and is very difficult to obtain for galaxies fainter than R = 24.5.

Another way to minimize the frequency of foreground contamination is to increase the spatial resolution of the LyC imaging, as the contamination rate is proportional to the area of the seeing disk. If one resolves the background galaxies (with half-light radii of 0.2″) instead of spreading the light over the typical seeing disk size (0.6″-1.0″), the contamination rate goes down by a factor of $\sim$ 9-25 and becomes almost negligible (Vanzella et al. 2012). This is the main reason that to robustly consider a galaxy as a clean LyC leaker, it should be detected with space based high resolution images like, Hubble SpaceTelescope (HST) images as well as be observed spectroscopicaly to

confirm its redshift.

Due to the limited success in LyC direct detection, many studies have tried to indirectly determine the escape fraction (e.g., Heckman et al. 2011; Jones et al. 2013b; Borthakur et al. 2014; Alexandroff et al. 2015; Erb 2015) based on the assumption of a "picket fence" model of the interstellar medium, where the foreground absorbing gas is assumed to be patchy, where parts of the galaxy are covered by opaque gas clouds and others are not. Thus, fesc is not dictated by a single column density of foreground gas, but is instead equal to the fraction of the galaxy not covered by opaque, neutral gas clouds. In this scenario, the covering fraction can be estimated using strong absorption lines from low ions (assumed to be co-spatial with neutral hydrogen), where the transmitted UV continuum in the saturated core of an absorption line (which would normally be zero for complete coverage) should give a good indication of the fraction of the UV disk that is transparent and, thus, the LyC escape fraction.

In chapter 2, We tested these indirect methods by attempting to detect escaping LyC with a 10-orbit Hubble near-UV (F275W) image that is just below the Lyman limit at the redshift of the Cosmic Horseshoe (a lensed galaxy at z=2.4). We concluded that the measured escape fraction is lower, by more than a factor of five, than the expected escape fraction based on the indirect methods. This emphasizes that indirect determinations should only be interpreted as upper-limits.

In chapter 3, we represent our results for identifying 4 clean LyC candidates at z$\sim$ 3.1 in SSA22 over density field, from a sample of 91 targeted star-forming galaxies with confirmed redshift of z $>$ 3.06 (based on their Ly$_\alpha$ emission line, Observed with Keck/LRIS) and HST/UVIS image coverage in both of the F336W and F814W filters that samples ionizing and non ionizing part of their spectra respectively. We matched 73 galaxies for which we had F814W detection at the location of redshift measurements, and after removing 7 galaxies that have foreground contamination, we build

a stack image including the 61 isolated objects without LyC detection in this sample from which we get the upper limit for the average escape fraction based on their flux ratios in the two filters. This is one of the biggest unbiased samples investigated, yet its average escape fraction is noticeably below the 0.2 limit, anticipated for the galaxies at the epoch of reionization. Indicating that we need to investigate even fainter, less massive galaxies in order to determine the role of star-forming galaxies at reionization of the universe.

Chapter 2

The Lyman Continuum Escape Fraction of The Cosmic Horseshoe: A Test of Indirect Estimates[†] *

Abstract

High redshift star-forming galaxies are likely responsible for the reionization of the Universe, yet direct detection of their escaping ionizing (Lyman continuum) photons has proven to be extremely challenging. In this study, we search for escaping Lyman continuum of the Cosmic Horseshoe, a gravitationally lensed, star-forming galaxy at z=2.38 with a large magnification of ~ 24. Transmission at wavelengths of low ionization interstellar absorption lines in the rest-frame ultraviolet suggest a patchy, partially transparent interstellar medium. This makes it an ideal candidate for direct detection of the Lyman continuum. We obtained a 10-orbit Hubble near-UV image using the WFC3/UVIS F275W filter that probes wavelengths just below the Lyman limit at the redshift of the Horseshoe in an attempt to detect escaping Lyman continuum radiation. After fully accounting for the uncertainties in the opacity of the intergalactic medium

as well as accounting for the charge transfer inefficiency in the WFC3 CCDs, we find a 3σ upper-limit for the relative escape fraction of $f_{esc,rel} < 0.08$. This value is a factor of five lower than the value (0.4) predicted by the 40% transmission in the low-ion absorption lines. Though possible, it is unlikely that the non-detection is due to a high opacity line of sight through the intergalactic medium ($< 20\%$ chance). We discuss several possible causes for the discrepancy between the escape fraction and the covering fraction and consider the implications for future attempts at both direct Lyman continuum detection as well as indirect estimates of the escape fraction.

2.1 Introduction

Star-forming galaxies are expected to be responsible for the reionization of the intergalactic hydrogen at $z > 7$ (e.g., Robertson et al., 2015) and much of the ionizing background at $3 < z < 7$ (Nestor et al., 2013; Becker and Bolton, 2013; Becker et al., 2015). Therefore, there has been much interest in quantifying the fraction of ionizing photons that escapes from star-forming galaxies (the "escape fraction," f_{esc}).

Recent measurements of the UV luminosity functions of galaxies (e.g. Oesch et al., 2013; Alavi et al., 2014; Bouwens et al., 2015b; Atek et al., 2015) have shown that galaxies can provide enough ionizing photons by $z \sim 6$ if the luminosity function is extrapolated to luminosities beyond our current detection limits and if the escape fraction is high (~ 0.2 or more Bouwens et al., 2012; Robertson et al., 2013, 2015; Bouwens et al., 2015a). However, the escape fraction is not well constrained, nor is the mechanism allowing for leakage of ionizing (Lyman continuum, LyC) photons. Unfortunately direct detection of the ionizing photons from galaxies at the epoch of reionization or soon thereafter is not feasible due to the high opacity of the intergalactic medium (IGM) at $z \gtrsim 4$ (Fan et al., 2006; Prochaska et al., 2009). Hence, over the last two

decades, many attempts have been made to detect escaping LyC from various types of star-forming galaxies at $z \lesssim 4$ (e.g. Leitherer et al., 1995; Steidel et al., 2001; Grimes et al., 2007, 2009; Siana et al., 2007, 2010, 2015; Cowie et al., 2009; Iwata et al., 2009; Bridge et al., 2010; Vanzella et al., 2010; Boutsia et al., 2011; Nestor et al., 2011, 2013; Mostardi et al., 2013; Guaita et al., 2016).

At $z < 2$, despite higher IGM transmission and lower foreground contamination rates, only 4 LyC emitters have been identified (Leitet et al., 2011, 2013; Borthakur et al., 2014; Izotov et al., 2016), with escape fractions less than 4% in three of the galaxies and $\sim$ 8% in the other. At $2 < z < 4$, ground-based studies have yielded many LyC-emitting candidates. However, after careful re-examination of many of them with higher resolution HST images, only three robust detections have been confirmed (Vanzella et al., 2012, 2015; de Barros et al., 2016; Mostardi et al., 2015; Vanzella et al., 2016).

Due to the limited success in LyC direct detection, many studies have tried to indirectly determine the escape fraction (e.g. Heckman et al., 2011; Jones et al., 2013b; Borthakur et al., 2014; Alexandroff et al., 2015; Erb, 2015) based on the assumption of a "picket fence" model of the interstellar medium, where the foreground absorbing gas is assumed to be patchy, where parts of the galaxy are covered by opaque gas clouds and others are not. Thus, f_{esc} is not dictated by a single column density of foreground gas, but is instead equal to the fraction of the galaxy not covered by opaque, *neutral* gas clouds. In this scenario, the covering fraction can be estimated using strong absorption lines from low ions (assumed to be cospatial with neutral hydrogen), where the transmitted UV continuum in the saturated core of an absorption line (which would normally be zero for complete coverage) should give a good indication of the fraction of the UV disk that is transparent and, thus, the LyC escape fraction.

The majority of ionizing photons are emitted by O-stars that are formed in dense

molecular clouds. Therefore, mechanisms to expose these stars must occur on relatively short timescales (within O-star lifetimes, < 10 Myr). This might be achieved either by SNe feedback (e.g. Dove et al., 2000; Fujita et al., 2003; Ma et al., 2015), interactions with other galaxies (Gnedin et al., 2008), or runaway massive stars (e.g., Conroy and Kratter, 2012). Although the details of the mechanisms by which LyC photons can escape the host galaxy are not well established, they can be distinguished on the basis of the morphological distribution of the escaping LyC in spatially resolved, directly-detected LyC emitters.

In this study we investigate the ionizing emission of J1148+1930, the "*Cosmic Horseshoe*" (Belokurov et al., 2007). The Horseshoe is a star-forming galaxy at $z = 2.38$ gravitationally lensed into an almost complete Einstein ring of $5''$ radius by a massive galaxy at $z = 0.44$. The magnification factor is 24 ± 2 (Dye et al., 2008). The high resolution, rest-frame UV spectrum of the Horseshoe has multiple, resolved interstellar absorption lines of low ions with depths of $\sim 60\%$ of the continuum flux density (Quider et al., 2009). As will be discussed in Section 2.4.2 and also in the Appendix, based upon these lines the picket fence model for the Horseshoe implies a rather high f_{esc}.

Thus, the Horseshoe is an excellent candidate from which to directly detect and study escaping LyC. In addition, its redshift is ideal for the study of LyC as the *Hubble Space Telescope* WFC3/UVIS F275W filter is only sensitive to the wavelengths short of rest-frame 912 Å. Specifically, 99.7% of its total integrated transmission is below the Horseshoe's Lyman limit at 3085 Å, this filter allows a direct measurement of LyC at wavelengths just below the Lyman limit, where the IGM opacity is at a minimum (Fig. 2.1, 2.2). Moreover, its large magnification provides a rare opportunity to study the Lyman continuum escape fraction with higher sensitivity and higher spatial resolution, which may allow us to distinguish between several possible LyC leakage mecha-

nisms.

In Section 2, we define our strategy to measure the escape fraction. In Section 3, we present the data. In section 4, we outline the method to overcome the detector degradations and artifacts that limit our sensitivity. Finally, in Section 5, we present the results and discuss their importance for future investigations of escaping LyC.

Throughout the paper, we adopt a cosmology with $\Omega_M = 0.3, \Omega_\Lambda = 0.7$ and $H_0 = 70$ km s^{-1} Mpc^{-1}. The flux densities are all in f_ν, i.e. are given in erg s^{-1} cm^{-2} Hz^{-1}, and the magnitudes are in the AB system.

2.2 Escape Fraction Definition

There are two widely used definitions of the escape fraction. First is the absolute escape fraction, $f_{esc,abs}$, defined as the fraction of emitted LyC photons that escapes into the IGM. This definition is convenient for theoretical models where one can translate star formation rates into intrinsic LyC flux, but difficult to measure observationally. To overcome the uncertainties of using the absolute escape fraction, Steidel et al. (2001) defined the relative escape fraction, $f_{esc,rel}$, as the fraction of escaping Lyman continuum photons divided by the fraction of escaping photons at rest-frame 1500 Å:

$$f_{esc,rel} = \frac{\left(F_{out}/F_{stel}\right)_{LyC}}{\left(F_{out}/F_{stel}\right)_{1500}} = \frac{f_{esc,abs}}{10^{-0.4A_{1500}}} \tag{2.1}$$

where F_{out} is the flux density (in F_ν) that escapes the host galaxy into the IGM, thereby contributing to the ionizing background and F_{stel} is the total intrinsic flux density produced in the galaxy. A_{1500} is the dust attenuation, in magnitudes, at 1500Å. For a Calzetti reddening law (Calzetti, 1997) we would have $A_{1500} = 10.33E(B-V)$. Rearranging the equation gives the commonly used equation for relative escape fraction

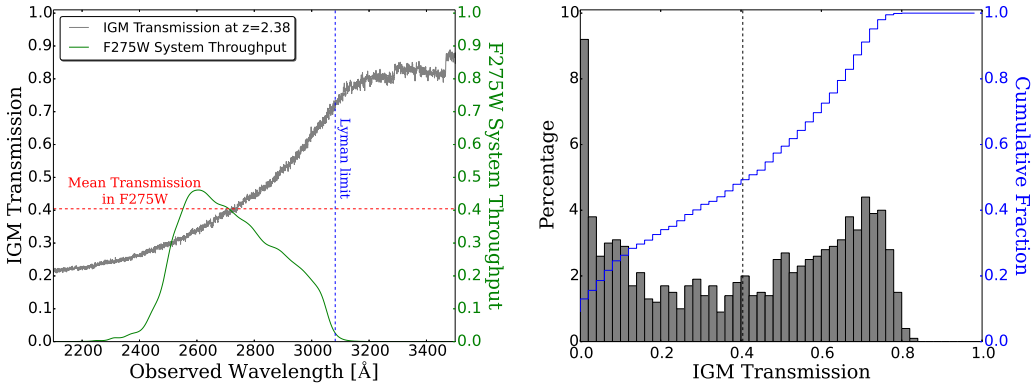

Figure 2.1: Left: The average transmission (from 1000 simulated LoS) of Lyman continuum photons through the IGM from galaxies at $z = 2.38$. The horizontal, red, dashed line indicates the F275W system throughput-weighted average IGM transmission (0.40). Right: A histogram of the F275W filter transmission-weighted IGM transmission of the 1000 simulated LoS. The vertical dashed line shows the same average transmission (0.4) through the filter and the blue line shows the cumulative fraction up to any given IGM transmission. We note that only ∼20% of the LoS have transmission below 8%.

(Siana et al., 2007):

$$f_{esc,rel} = \frac{\left(F_{1500}/F_{LyC}\right)_{stel}}{\left(F_{1500}/F_{LyC}\right)_{obs}} \times e^{\tau_{H_{I,IGM}}} \tag{2.2}$$

where $\tau_{H_{I,IGM}}$ is the optical depth of the Lyman line and continuum absorption of the neutral intergalactic hydrogen along the line of sight (hereafter LoS), $(F_{1500}/F_{LyC})_{stel}$ is the intrinsic flux decrement across the Lyman break, and $(F_{1500}/F_{LyC})_{obs}$ is the corresponding observed ratio. Eq. 3.2 is useful as it does not require knowledge of dust attenuation and the 1500 Å flux density of high redshift galaxies can be easily measured.

In order to assess the escape fraction of a galaxy we have to estimate those three values. The intrinsic flux ratio depends on age, star formation history, initial mass function (IMF) and metallicity of the stellar populations. In Siana et al. (2007, their Fig 1) this ratio is calculated at both $\lambda_{rest} = 700$ Å and $\lambda_{rest} = 900$ Å for an instantaneous

burst and continuous star formation, and using stellar population synthesis models from both Bruzual and Charlot (2003) and Leitherer et al. (1999).

To estimate the average transmission of the IGM, we ran a Monte Carlo simulation (see Siana et al., 2007, for details) using the known distributions of HI absorber column densities as a function of redshift (Janknecht et al., 2006; Rao et al., 2006; Ribaudo et al., 2011; O'Meara et al., 2013) as summarized in Table 2 of Alavi et al. (2014). We simulate 1000 LoSs through the IGM to $z = 2.38$. Each LoS gives the transmission as a function of wavelength, from which we determine average transmission through the F275W filter as illustrated by the left panel of Fig. 2.1. The right panel of Fig. 2.1 shows the distribution of IGM transmission through the F275W filter for all 1000 LoS, demonstrating significant variation. In fact, the mean value of $\exp(-\tau_{IGM}) = 0.4$ is not a common value, as the distribution is bimodal. This can be converted to the distribution of escape fraction which will give the probability of each escape fraction limit. Also Rudie et al. (2013), showed considering the higher incidence of the absorbers in the circumgalactic medium (CGM) can reduce the average transmission of CGM +IGM by a factor of $\sim 10\%$ compared to the average transmission of only IGM, yet they still have a higher mean transmission estimate.

With estimates of the intrinsic Lyman break amplitude, $(F_{1500}/F_{LyC})_{stel} \sim 7$, and the mean IGM transmission, $\exp(-\tau_{IGM}) = 0.4$, we need only to measure the flux density ratio, $(F_{1500}/F_{LyC})_{obs}$, to determine the relative escape fraction. The consequences of variations in the IGM opacity are discussed in Section 2.4.2.

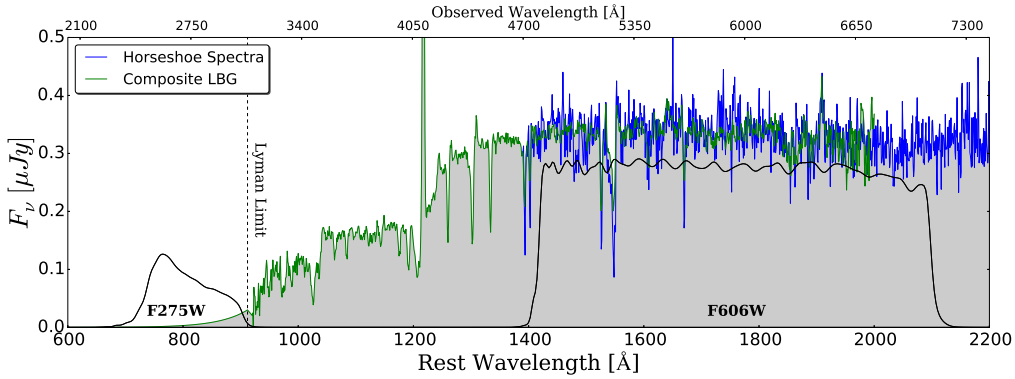

Figure 2.2: The green line is the composite spectrum of $z \sim 3$ LBGs from Shapley et al. (2003), shifted to the Horseshoe's redshift, $z = 2.38$. The blue line is the smoothed spectrum of the Horseshoe from Quider et al. (2009). The spectrum below the Lyman limit is just an illustrative extrapolation assuming a constant f_ν corrected for the mean IGM transmission from $z = 2.38$ at each wavelength, i.e. $exp(-\tau_{IGM})$. Also plotted are the total system throughput for the two WFC3/UVIS F275W and F606W filters, which sample, respectively, the ionizing and non-ionizing UV continua.

2.3 Observations and Data Reduction

2.3.1 Observations

For our analysis, we have used two images from the *Hubble Space Telescope* Wide Field Camera 3 (WFC3) UV channel (UVIS). First, we used a one-orbit (2412 s) image in the F606W filter from the Hubble Program ID 11602 to measure the non-ionizing UV flux density at $\lambda_{rest} \sim 1800$ Å.

Because the rest-UV SED is nearly flat in f_ν ($g - i = 0.04$ AB, Belokurov et al., 2007), we assume that the flux density at 1500 Å (typically used for escape fraction measurements) is the same as the flux density at 1800 Å.

We obtained a 10-orbit image in the F275W filter to sample the rest-frame LyC, (transmission-weighted wavelength of 2704 Å, or 800 Å in the rest frame of the Horseshoe). Fig. 2.2 shows these filter transmission curves with a typical Lyman break galaxy, LBG spectrum at $z = 2.38$ and the smoothed spectrum of Quider et al. (2009).

Below 4000 Å, read noise is the main source of noise in our UVIS imaging, although, for more recent UVIS observations, the dark current has become more important. Hence, to minimize the number of readouts, the F275W exposure times were half an orbit in duration (1404 s), with a total of 20 exposures and total exposure time of 28080 s.

The UVIS CCDs suffer from significant charge transfer inefficiency (CTI) when both the background and the targets are faint (MacKenty and Smith, 2012). As there is effectively no sky background in F275W ($\sim 0.35\ e^-$ per pixel per half orbit exposure), the dark current ($\sim 1.5\ e^-$ per pixel per half orbit exposure) dominates the total background but is very low. In addition, the expected LyC signal is very faint. Therefore, CTI is of particular concern for these observations and we have to understand its effects on our measurements. In order to minimize the number of pixels traversed by the electrons upon readout, and therefore reduce the charge transfer inefficiency, we intentionally placed the Horseshoe closer to the readout edge of the detector, with its center $\sim$ 40% of the CCD width from the read-out edge. In F606W, both the high signal and high background minimize CTI, so it will not significantly affect our measurements in that filter.

2.3.2 Data Reduction

Part of the WFC3/UVIS calibration process is the subtraction of a dark reference file to correct dark current structure and flag hot pixels that can cause significant artifacts in the images. The current standard processing of the dark calibration is insufficient for the WFC3/UVIS data of this program due to the radiation damage causing poor charge transfer efficiency (CTE), and the low background levels in the F275W filter. The STScI dark frames have the following inadequacies: First, the STScI process uses an outdated

definition of a hot pixel that has not been updated to account for CTE degradation, resulting in unmasked warm-to-hot pixels remaining. Second, the standard processing uses the median value of the average darks as the value of all pixels in the dark frame. This median dark file is not suitable for the low background of the NUV, because it leaves a low-level gradient and a blotchy pattern in the dark that is not subtracted. Lastly, the STScI darks are not corrected for CTE, furthering the improper hot pixel masking, and contributing to incorrect median levels in the STScI darks.

To solve these issues, custom CTE-corrected superdarks are created in a two step process as detailed in Rafelski et al. (2015). First, all darks from a 4 day window at the same cadence as the STScI darks are used to create a superdark, where the background is modeled with a third order polynomial to remove the background gradient temporarily to find the hot pixels with a uniform updated threshold level. This step is necessary due to the large number of new hot pixels per day, and the drastic change in hot pixels after each anneal, where the CCD is warmed up for several hours to reduce the number of hot pixels caused by radiation damage. Then, all darks from a single anneal cycle are averaged together avoiding the hot pixels from each 4 day window, to determine the actual dark level for each good pixel. This averaged background is then used in conjunction with the hot pixel map from the first step to create a new superdark which is used for calibrating the science exposures. These new darks properly flag the hot pixels, remove the background gradient, and significantly reduce the blotchy pattern in the science exposures.

We first CTE-corrected and dark subtracted all of the flat fielded images. We then used the AstroDrizzle package (Gonzaga et al., 2012), provided by the Space Telescope Science Institute, to combine the dithered images into a final image with a $0.04''$ pixel scale. AstroDrizzle outputs inverse variance maps which were used to determine the expected Poisson uncertainties in each pixel. The alignment of individual exposures was

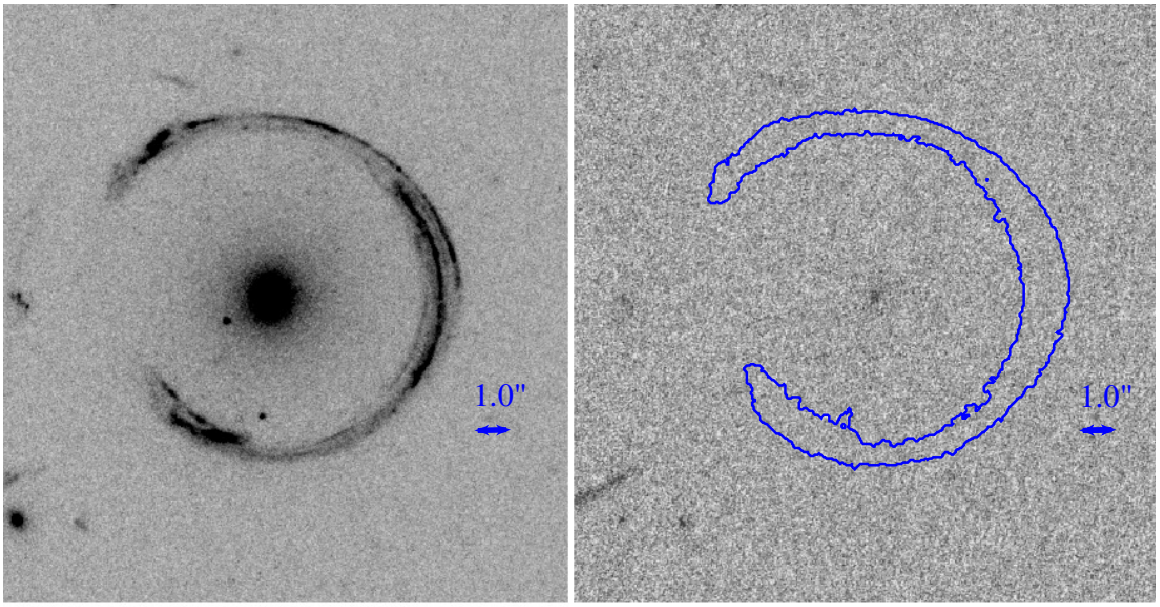

Figure 2.3: Left: The 1-orbit F606W image sampling the non-ionizing flux at $\lambda_{rest} \sim$ 1800 Å. Right: The 10-orbit F275W image, with our largest aperture depicted in blue (the "L" aperture, defined by a low surface brightness isophote in the F606W image). The Horseshoe is lensed into an almost complete Einstein ring with 5″ radius ($\sim$ 125 pixels).

accurate to $<$ 4 mas in both filters. After combining all images, we subtracted a slight, residual background gradient in the read-out direction by fitting a third-order polynomial to both CCDs in order to guarantee a uniform background around the Horseshoe.

The reduced images in both filters are shown in Fig. 2.3. To determine the image depths, we corrected the pixel rms for the adjacent pixel correlations based on Casertano et al. (2000) (in our case, multiplied by 1.5) to estimate sigma per pixel. The derived 5σ image depths in an aperture with a 0.4″ radius are 27.34 and 26.79 AB magnitude for the F606W and F275W images, respectively. We note that this depth does not reflect the CTI that will be discussed later and affects the calculated upper limit on f_{esc}.

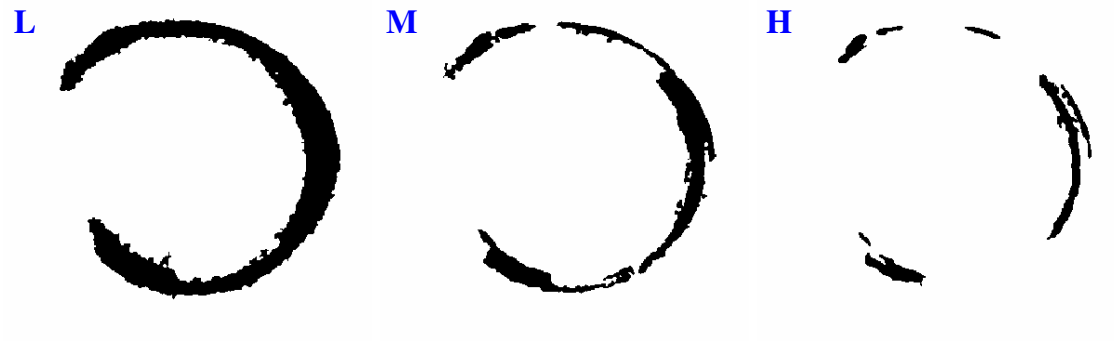

Figure 2.4: The "L" ,"M" and "H" apertures defined by low, medium and high surface brightness isophotes in the F606W image (1.3, 3 and 5 σ above the background, respectively).

2.3.3 Photometry

We searched for F275W (LyC) flux in a number of apertures defined by isophotes of varying F606W (non-ionizing UV) surface brightness, because it is possible that LyC is only escaping from certain regions (like those of high star formation surface density, for example). We used three apertures with boundaries defined by low (L), medium (M), and high (H) surface brightness isophotes, corresponding to 1.3σ, 3σ, and 5σ above the background in F606W. These apertures constitute a range from a near-total flux aperture up to a high surface brightness aperture and are displayed in Fig. 2.4. No signal is detected through the F275W filter in any of the apertures.The F275W S/N in these apertures varies between -1.2 to $+1.1$, and is therefore not a significant detection.

We can use the depths of the F275W image to place upper limits on the LyC escape fraction. However, first, we must assess the effect (if any) of CTI as it may move some of the expected flux out of our aperture, erasing some of the signal. Teplitz et al. (2013) has shown cases where the signal can be lost completely in smaller apertures. Unfortunately, at the time the data were taken the "post flash" option (Biretta and Baggett, 2013) to add background to the image was not available to mitigate CTI, and pixel-based empirical corrections of CTI are impossible in reconstructing images if no

signal has remained. Therefore, our images in the F275W filter will be affected by CTI.

sectionMethod to Account for CTI As mentioned above, we do not detect a significant LyC signal in the F275W image. However, it is possible that the depth of the image was significantly affected by CTI. If that is the case, we can calculate the threshold flux above which we should have detected the signal from the Horseshoe, including the effects of CTI. To account for CTI we should either be able to correct for it or simulate its effect on our assumed images. As the signal is essentially lost in our LyC filter, there is not enough flux to make a correction feasible. Therefore, we must forward-model the effects of CTI, to determine a flux threshold, above which we would have detected the Horseshoe despite CTI. For this analysis, we use the "CTE forward" code released by STScI [1], which simulates the effects of CTI on a provided image.

2.3.4 Finding the Detection Limit

We first make an "ideal" image in the F275W filter, add the expected background, simulate the effect of CTE, and finally add the read-noise to produce an individual F275W exposure. We then add them to produce a simulated full-depth F275W image. Below we discuss details of each of these steps.

Assumed image

Because we do not know the morphology of the escaping LyC, we naively assume that the LyC has a similar morphology to that of the non-ionizing UV continuum in the F606W image. We then simply scale the flux from the F606W image down to simulate F275W images of various fluxes. Because the F606W and F275W images were taken at different orientation angles (relative to the read-out directions), we also

[1] http://www.stsci.edu/hst/wfc3/tools/cte_tools

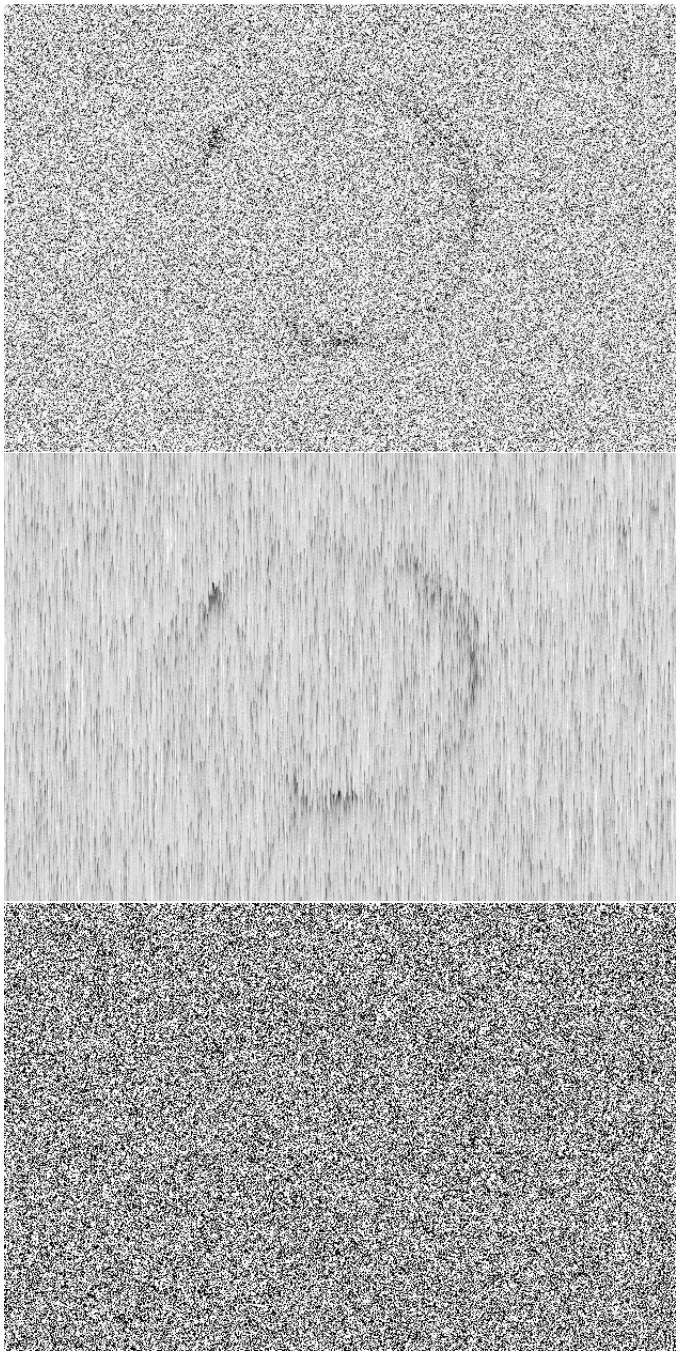

Figure 2.5: This figure demonstrates how signal can be lost due to charge transfer inefficiency of the WFC3/UVIS CCD. Top: An assumed F275W (LyC) image based on the F606W image scaled down by 6 magnitudes with a typical background (dark+sky). Middle: The effect of CTI has been added based on the CTE Forward code provided by STScI. The effect of CTI is clear, as it has smeared the signal in the read-out (vertical) direction. Bottom: The simulated image is shown after adding read noise (which is not affected by CTE).

rotate the F606W image of the Horseshoe and place it in the same location as the expected position in the F275W image.

Background

The CTI is very sensitive to the background level. Even a small background is effective at partially occupying the electron traps, resulting in reduced CTI. Therefore, it is imperative to carefully assess and add the background (sky + dark) electrons to our image before implementing the CTI effects. We calculate the dark current and sky backgrounds to be 1.53 e^- pix^{-1} exposure^{-1} and 0.35 e^- pix^{-1} exposure^{-1} respectively. Therefore, we assume a background with a Poisson distribution with an average of 1.88 e^- pix^{-1} exposure^{-1}.

Charge Transfer Phase and Read-noise

To simulate the effect of CTE on our simulated images we ran the CTE-Forward code provide by STScI, assuming various total LyC fluxes. Afterward, the read noise was added to each pixel as a random number with a Gaussian distribution with a standard deviation of 3.0, consistent with the read noise for the four WFC3/UVIS amplifiers. This results in a simulated image which is a statistical representation of what would have been observed by the CCD, albeit without accounting for cosmic rays.

Stacking the Images

We simulated 20 of these F275W images and stacked them to obtain a full-depth stacked simulated image. Now we are able to investigate whether, for an assumed LyC flux, the Horseshoe would be detected with 3σ confidence in our three different apertures.

Of course, our “detection level" derived above is noisy, because it relies only on a single simulated stacked image, and the signal in this image will, by definition, vary by the input standard deviation multiplied by the square root of the number of pixels. Therefore, to more accurately assess the expected detection threshold, we produce five instances of these simulated images at the same LyC flux level and use the average of their detection levels. We had to using a higher S/N background, because the Poisson variations in the background are large compared to the background and such variations can affect the level of CTI in each pixel.

2.4 Results and Discussion

2.4.1 Observed Flux Ratios

We generated simulated images with eight different input magnitudes, spanning a range of two magnitudes with steps of 0.25 magnitude (close to where we expect to have 3σ detection within our apertures). For each of the stacked simulated images, after removing the background, we measured the level of signal and noise within each aperture. Fig. 2.6 shows the measured S/N of each of the images in the three apertures, as a function of the input magnitude within that aperture. For each of the input magnitudes, the average S/N is then plotted as filled circles. To find the input magnitude that results in a 3σ detection, we fit a curve to the filled circles, assuming that input flux is linearly proportional to the detection level, and determine at what magnitude the significance of the detection would be greater than $S/N > 3$. These threshold magnitudes and the corresponding F606W magnitudes are listed in Table 2.1. All magnitudes have been corrected for Galactic extinction at the location of the Horseshoe

Table 2.1: The characteristics and measured quantities in each aperture

Apertures	**L**	**M**	**H**
σ above background in F606W [a]	1.3	3.0	5.0
number of pixels	14302	7514	3278
magnitude in F606W	19.83	20.12	20.62
detection level in F275W	-1.23	-0.99	1.08
3 σ limiting magnitude in F275W image [b]	25.82	26.17	26.62
$f_{esc,rel}$ for limiting magnitude	0.079	0.075	0.078
3 σ threshhold magnitude in F275W [c]	25.82	26.11	26.45
$f_{esc,rel}$ for threshold magnitude	0.079	0.079	0.092

a The selection criteria to choose the apertures.
b Based on the depth of the image.
c Based on Fig. 2.6.

based on Schlafly and Finkbeiner (2011) ($A_{F275W} = 0.258$ mags and $A_{F606W} = 0.117$ mags).

For comparison, we have also listed in Table 2.1 the escape fraction limits based solely on the background noise and not considering signal loss due to CTI. Interestingly, the limits are very similar, meaning that the CTI losses are not large for our measurements. The CTI results in 0%, 5%, and 17% increase in the limiting flux respectively for L, M, and H apertures. Not surprisingly, the CTI effect on photometry is not significant in the largest apertures, as the typical trapped e^- is released < 10 pixels behind the original pixel (Rafelski et al., 2015). Therefore, CTI losses in the photometry only become a concern when the aperture width (in the readout direction) approach this length scale.

2.4.2 Escape Fraction

With the F275W 3σ threshold magnitudes and the F606W magnitudes in the corresponding apertures, we can calculate the limits on the non-ionizing to ionizing flux

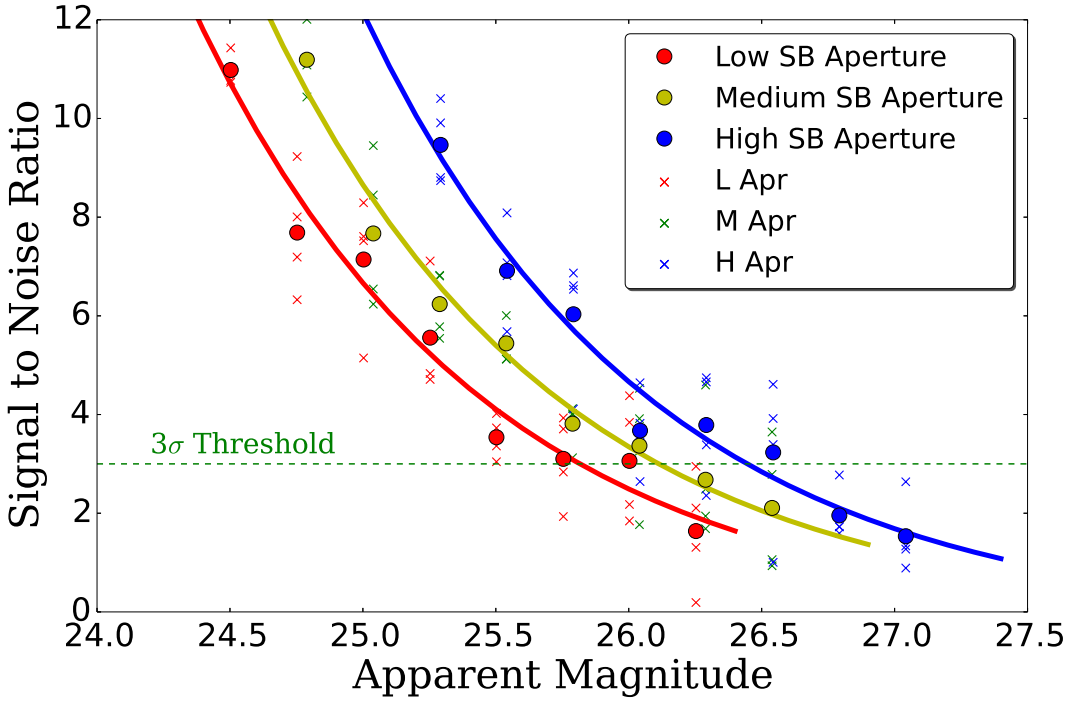

Figure 2.6: The measured signal to noise ratios of simulated images ($\times$ symbols) as a function of input F275W magnitudes, for the three apertures L (red), M (green) and H (blue). For each of the input magnitudes the average detection levels are shown with filled circles in the corresponding color. For each aperture we fit a curve (solid lines) to the average values to determine at what magnitude the signal would be detected at 3 σ. These "threshold magnitudes" for each aperture are also listed in Table 2.1.

ratio and, ultimately, the relative escape fraction, using Eq. 3.2. In Table 2.1, we list the 3σ limits on the relative escape fraction in all three apertures.

After including the effects of CTI, the upper limits on the relative escape fraction in each aperture are similar: 0.079, 0.079, and 0.092 in the L, M and H apertures, respectively, as the significant reduction in F275W noise in smaller apertures is offset by reduced F606W flux. Using a Calzetti extinction curve (Calzetti, 1997) and $E_{(B-V)} = 0.15$ (Quider et al., 2009), we convert $f_{esc,rel} < 0.08$ to $f_{esc,abs} < 0.02$, well below the average value needed to maintain ionization at $z \sim 7$ ($f_{esc,abs} \sim 0.2$) (e.g., Robertson et al., 2015; Bouwens et al., 2015a).

As mentioned in Section 2.1, the high resolution, rest-frame UV spectrum of the Horseshoe has multiple, resolved interstellar absorption lines of low ions with depths of $\sim$ 60% of the continuum flux density (Quider et al., 2009). Some of these lines are shown in Fig. 2.7. These lines have very different oscillator strengths but similar absorption depths, especially for the case of Si II transitions, which all originate from the same ion and the relative depths are therefore independent of the metallicity or ionization. Quider et al. (2009) therefore conclude that the depth of the lines is not due to the column density of a foreground screen. Rather, the depth is dictated by the fraction of the UV-bright disk that is covered by clouds that are opaque in these lines. Hence for the Horseshoe, we expect a ~ 0.6 "covering fraction" of low-ionization gas where neutral hydrogen would reside. Based on the picket fence model and the discussion in the Appendix, this in turn implies $f_{esc,rel} \sim 0.4$.

The reported 3σ limits in our apertures of $f_{esc,rel} < 0.08$ are roughly five times lower than the expected escape fraction inferred from the depth of the low-ion absorption lines in the spectrum of the Horseshoe. One reason for this discrepancy could be the existence of a rather opaque IGM along the LoS to the Horseshoe. To obtain our measured $f_{esc,rel}$ we adopt the average transmission of the IGM through the F275W fil-

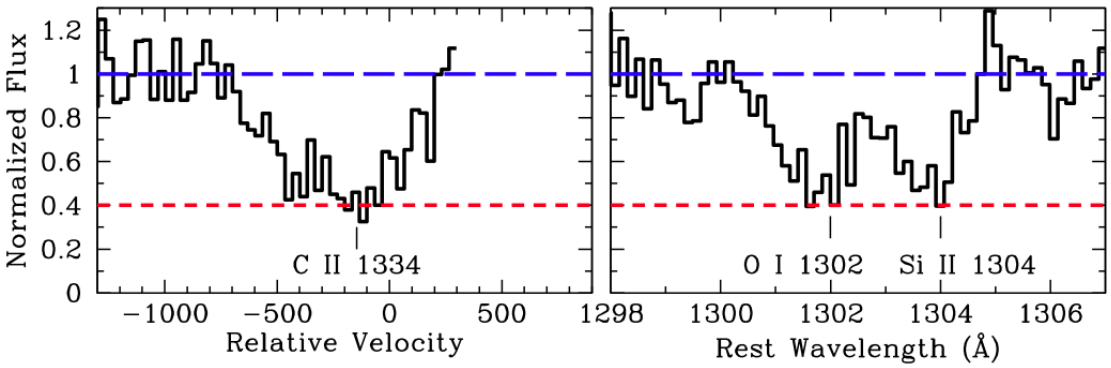

Figure 2.7: Three low ionization absorption line profiles from the high resolution ($R \sim 4000$) spectrum of the Horseshoe (Quider et al., 2009). Though these ions have different abundances, and the transitions have different oscillator strengths, the depth of each feature is the same, ~ 0.4 of the continuum flux density, suggesting a covering fraction of ~ 0.6 for the low-ionization gas. As this low-ionization gas is also where neutral hydrogen would reside, this could imply that as much as 40% of the UV-bright disk may be unobscured, allowing LyC photons to escape along those sight lines.

ter ($e^{-\tau_{H_{I,IGM}}} = 0.402$). But, as is evident in Figure 2.1, this value is not representative of the nearly bimodal distribution of the IGM transmission. Specifically, there is an almost 20% chance that the Horseshoe lies along a line of sight that is at least 5× more opaque than the average transmission assumed here (less than 0.08), which could thus explain our non-detection, even if $f_{esc,rel}$ is 0.4 as suggested by the depth of the low ionization interstellar absorption lines. On the other hand, the IGM transmission could also be significantly higher than the average value, in which case our $f_{esc,rel}$ limit would be even lower.

There are still a number of additional possible causes for a discrepancy between the transmission in the low ions and the relative escape fraction. Many of these reasons have been mentioned by Jones et al. (2013b), but we discuss them here in the context of the Horseshoe;

1. The absorption depths of the low-ions give only a covering fraction of the *non-ionizing* UV disk (from $\sim 1250 - 1700$ Å). However, because the LyC-emitting regions

are short-lived, they likely comprise only a subset of the area that is emitting non-ionizing UV light. Therefore, a clear line of sight toward a non-ionizing UV-emitting region does not necessarily imply that LyC photons will escape. Furthermore, it is likely that the LyC-emitting regions have *higher* columns of dust and gas toward them, as they are younger and more embedded in their birth clouds. Indeed, this is the reason that extinction of H II regions is typically higher than extinction of other regions at the same wavelengths (Calzetti, 1997). Therefore, the transmitted emission in the low-ion absorption lines should be considered an upper-limit to the possible LyC escape fraction.

2. The LyC absorption by hydrogen acts at all wavelengths below the Lyman limit, whereas the absorption lines absorb at one specific wavelength. Therefore, one must be careful in interpreting the absorption lines. The velocity structure of the absorbing gas is critical when converting the depth of the absorption lines to covering fractions. For example, if half of the galaxy is covered by gas outflowing at 0-100 km s^{-1}, and the other half is covered by gas outflowing at 100-200 km s^{-1}, then the depth of the absorption line (in a high-resolution spectrum) will never be more than 50% of the continuum. However, the LyC in such a scenario would be 100% absorbed because it is insensitive to the velocity of the outflow. Thus, once again, the LyC escape fraction should generally be lower than the absorption line depth.

3. If there are foreground neutral clumps with low velocity dispersion that are not resolved in wavelength, the profile of the absorption line will be smoothed, and the measured transmission will reflect only an upper limit on $f_{esc,rel}$. In our case the Keck/Echellette Spectrograph and Imager (ESI) spectra of the Horseshoe has the resolution of $\sim$ 75 km s^{-1}. Though the velocity width of the absorption profiles is much larger than this value, it is still possible that there exists unresolved narrow components.

4. If the LyC absorbing gas is very low metallicity (Fumagalli et al., 2011) perhaps because it is inflowing from the IGM, then the metal line absorption will not be strong, but the hydrogen opacity will still be large and can absorb the LyC. Though, given the significant amount of enriched outlawing material, and the large accumulated stellar mass, it seems unlikely that a significant fraction of the absorbing gas would be very low metallicity. However, in such a scenario, the absorption line transmission should be treated as an upper limit.

Because of the reasons outlined above, we believe a non-uniform coverage of low-ionization metals is a necessary, but not sufficient, condition for significant escape of Lyman continuum. Hence, any estimates of $f_{esc,rel}$ based on these absorption lines should be interpreted as upper-limits.

Although $f_{esc,rel}$ may be significantly lower than predicted by the transmission in low-ion absorption lines, it is worth noting that the two values will be better correlated in more compact galaxies because many of the issues raised above that can cause the two to differ are mitigated significantly if the galaxy is extremely compact (< 100 pc). First, the ionizing and non-ionizing UV continua are likely emitted from the same regions (a single star-forming region). In contrast, in a large galaxy, much of the non-ionizing flux is likely emitted from regions with no current star formation (and thus no LyC production). Second, the smaller the galaxy, the likelier it is that the absorption of light from different parts of the galaxy is caused by the same absorbers, especially if the galaxy size approaches the typical size of an absorbing neutral clump in the ISM or CGM. Thus, one has to worry less about clumps of different velocities covering different parts of the disk.

Indeed, Heckman et al. (2011); Borthakur et al. (2014); Alexandroff et al. (2015) have been investigating the relative escape fraction, both directly and indirectly from luminous and extremely compact galaxies, which they refer to as dominant central

objects (DCOs, ionizing UV sizes of < 100 pc). Thus, it may be true that the absorption line transmission reasonably predicts the relative escape fraction in these galaxies, but it may not be the case in all galaxies.

The intrinsic size of the Cosmic Horseshoe galaxy has been measured in both the non-ionizing UV and Hα by Jones et al. (2013a). In both cases, the emission is coming from an elongated region that is ~ 0.2 kpc $\times 0.4$ kpc, significantly smaller than the average UV size of galaxies of similar luminosity which typically have diameters of $\sim 3-4$ kpc (Law et al., 2007). With such a small area, we might expect that some of the issues above would be mitigated. However, this area is still large enough that it likely consists of many distinct star-forming regions, and may still be covered by a range of clump distributions along the LoS. To understand the efficacy of these indirect estimates of $f_{esc,rel}$, we must directly image the LyC of a large sample of galaxies with high transmission in the low-ion absorption lines.

2.5 Summary and Conclusion

In this study, we have attempted to measure the Lyman continuum escape fraction of the Cosmic Horseshoe, a highly magnified, star-forming galaxy at $z = 2.38$. The high resolution rest-frame ultraviolet spectrum of the Horseshoe shows only $\sim 60\%$ absorption in the resolved interstellar absorption lines of low ions (e.g. OI, CII, SiII), suggesting a patchy foreground neutral gas distribution (Quider et al., 2009) and a relative escape fraction of $f_{esc,rel} = 0.4$. Given the high magnification, the well-suited redshift for the existing WFC3/UVIS filters, and the suggestion of a partially transparent foreground gas distribution, we obtained a 10 orbit image of the Lyman continuum (at ~ 800Å) with the WFC3/UVIS F275W filter.

We made and subtracted enhanced darks that contain the structure seen in the actual darks. We then forward modeled the effects of charge transfer inefficiency of the WFC3/UVIS CCDs to determine at what flux density we would no longer be able to detect the LyC. Because the photometric apertures are large (relative to unlensed galaxies), we find that the effects of charge transfer inefficiency on our photometry are quite small (17% affect to the LyC photometry in the smallest [worst case] aperture).

We do not detect significant LyC flux from the Cosmic Horseshoe, and the flux density limit gives an upper limit on the relative escape fraction of $f_{esc,rel} < 0.08$ (3σ) when assuming average transmission through the IGM. The upper limit is a factor of five lower than the value suggested by the significant transmission in the low-ion interstellar absorption lines. This suggests that the transmission in the interstellar absorption lines may not be a reliable proxy for the relative escape fraction (though cf. Borthakur et al., 2014). We outline a number of reasons why the transmission in the absorption lines of low ions may only give an upper limit to the escape fraction. Finally, we note that there is a 20% chance that the transmission of the IGM along the line of sight to the Horseshoe may be five times lower than the assumed average, which would fully explain our non-detection even if the relative escape fraction were 0.4. A study of a much larger sample of star-forming galaxies can statistically overcome the uncertain IGM transmission, and would definitively test the indirect method of measuring the escape fraction via the depths of the interstellar absorption lines.

2.6 Appendix A: Covering Fraction to Escape Fraction

There are a number of definitions of the LyC escape fraction in the literature, “relative escape fraction”, “absolute escape fraction”, “dust free escape fraction”, etc.. This has lead to some confusion about how they are related to the physical covering fraction

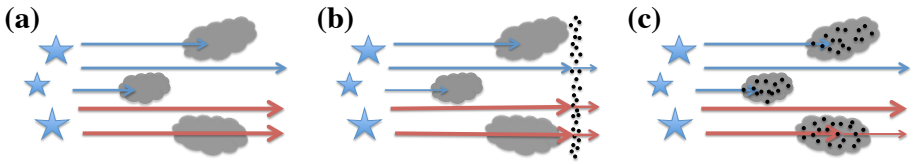

Figure 2.8: The three simple models for the distribution of dust within a patchy ISM/CGM arm depicted: (a) no dust; (b) a uniform dust screen, (c) dust only within the gas clumps. The ionizing and non-ionizing fluxes are represented by blue and red arrows, respectively.

or the depth of the low-ionizing absorption lines. To avoid this confusion, we derive here what exactly each of these terms represents for three simplified scenarios of dust distribution within a patchy ISM. These simplified cases are a) a dust free model; b) a uniform screen of dust and c) dust only located in dense clouds. Cartoons of these models are shown in Figure 3.13 where dusty regions are shown as solid black dots. We note that the precise location of the uniform dust screen in model (b) does not affect the calculations below.

We also note that the covering fraction inferred by the depth of the absorption (denoted here by $C_{F'}$) is not necessarily the same as the physical covering fraction of the dense clouds (C_F). Observationally, we can only measure $C_{F'}$ which is defined as the ratio of the observed flux density at the wavelength of the absorption line (assumed to be completely saturated in the dense clouds), to the observed continuum flux density (at around 1500Å): $1 - C_{F'} = \frac{F_{line,obs}}{Fcont,obs}$. Therefore, we report our escape fractions as a function of $C_{F'}$:

2.6.1 Case (a) No Dust :

For the dust free case, the LyC flux density and the flux density in the absorption lines get completely absorbed by the clouds while the 1500 Å continuum flux density remains unaffected by the gas clouds:

$$F_{LyC,out} = F_{LyC,stel} \times (1 - C_F); F_{1500,out} = F_{1500,stel} \tag{2.3}$$

$$1 - C_{F'} = \frac{F_{line,obs}}{F_{cont,obs}} = \frac{F_{1500,stel} \times (1 - C_F)}{F_{1500,stel}} = 1 - C_F \tag{2.4}$$

So here $C_F = C_{F'}$, which results in:

$$f_{esc,rel} = \frac{\left(F_{LyC}/F_{1500}\right)_{out}}{\left(F_{LyC}/F_{1500}\right)_{stel}} = 1 - C_F = 1 - C_{F'} \tag{2.5}$$

$$f_{esc,abs} = \frac{F_{LyC,out}}{F_{LyC,stel}} = 1 - C_F = 1 - C_{F'} \tag{2.6}$$

In this case, $f_{esc,rel}$ and $f_{esc,abs}$ are the same. In the literature, this is sometimes referred to as the dust free escape fraction.

2.6.2 Case (b) Screening Dust :

In this case we add a layer of uniform dust to the previous geometry. So all the flux densities are now the dust attenuated fluxes of the previous case:

$$F_{LyC,out} = F_{LyC,stel} \times (1 - C_F) \times e^{-\tau_{dust,LyC}}; F_{1500,out} = F_{1500,stel} \times e^{-\tau_{dust,LyC}} \tag{2.7}$$

$$1 - C_{F'} = \frac{F_{line,obs}}{F_{cont,obs}} = \frac{F_{1500,stel} \times (1 - C_F)}{F_{1500,stel}} = 1 - C_F \tag{2.8}$$

Again in this geometry we have $C_F = C_{F'}$, which results in:

$$f_{esc,rel} = \frac{\left(F_{LyC}/F_{1500}\right)_{out}}{\left(F_{LyC}/F_{1500}\right)_{stel}} = 1 - C_{F'} \times e^{-(\tau_{dust,LyC} - \tau_{dust,1500})} \tag{2.9}$$

$$f_{esc,abs} = \frac{F_{LyC,out}}{F_{LyC,stel}} = 1 - C_{F'} \times e^{-\tau_{dust,LyC}} \tag{2.10}$$

Here neither $f_{esc,rel}$ nor $f_{esc,abs}$ are not equivalent to the $1 - C_{F'}$.

2.6.3 Case (c) Dust in Clouds:

In this case the dust closely traces the dense gas. We believe that this is the model that most closely resembles reality, as any significant dust will be accompanied by opaque columns of gas (both in the LyC and the interstellar absorption lines, Gnedin et al., 2008). Though the dust has practically no effect on the line or LyC flux (they get absorbed predominantly by the gas), it attenuates the observed continuum flux. So we have:

$$F_{LyC,out} = F_{LyC,stel} \times (1 - C_F); F_{1500,out} = F_{1500,stel} \times (1 - C_F + C_F \times e^{-\tau_{dust,1500}}) \tag{2.11}$$

$$1 - C_{F'} = \frac{F_{line,obs}}{F_{cont,obs}} = \frac{F_{1500,stel} \times (1 - C_F)}{F_{1500,stel} \times (1 - C_F + C_F \times e^{-\tau_{dust,1500}})} \neq 1 - C_F \tag{2.12}$$

Interestingly, in such a scenario the covering fraction based on the depth of the low ionization absorption lines is actually different from the physical covering fraction, i.e. $C_F \neq C_{F'}$. As such we end up with the following relations for the escape fractions:

$$f_{esc,rel} = \frac{\left(F_{LyC}/F_{1500}\right)_{out}}{\left(F_{LyC}/F_{1500}\right)_{stel}} = 1 - C_{F'} \tag{2.13}$$

$$f_{esc,abs} = \frac{F_{LyC,out}}{F_{LyC,stel}} = 1 - C_F = 1 - \frac{C_{F'}}{C_{F'} + (1 - C_{F'}) \times e^{-\tau_{dust,1500}}} \tag{2.14}$$

Therefore, $f_{esc,rel}$ is, in fact, equal to the ratio of the observed flux density in the line to the observed continuum flux density, $f_{esc,rel} = 1 - C_{F'}$. Since $1 - C_{F'}$ is a common observable, it is best to compare this measurement to that of $f_{esc,rel}$ as we have done in this work.

Chapter 3

The Lyman Continuum Escape Fraction of The Candidate Galaxies in SSA22

Abstract

High-redshift star-forming galaxies are likely responsible for the reionization of the Universe, yet only a few cases of direct detection of their escaping ionizing (Lyman continuum) photons have been robustly observed and the majority of them in the last two years. In this study, we report four strong candidates for the escaping Lyman continuum in the SSA22 over density proto-cluster around z=3.09. The over density of star-forming galaxies at z>3.06 insures that we can directly sample their Lyman continuum using Hubble's near-UV image using the WFC3/UVIS F336W filter that probes wavelengths just below the Lyman limit at the redshift above 3.06 where the over density is located. After fully accounting for the uncertainties in the opacity of the intergalactic medium(IGM) as well as accounting for the charge transfer inefficiency(CTI) in the WFC3 CCDs, for our sample we find a 1σ upper-limit for the relative escape fraction of $f_{esc,rel} < 0.08$ and $f_{esc,rel} < 0.11$ for cases with and without direct detection. This value is still less than that of the estimated average value required if the galaxies

where to provide the ionizing photons for the reionization of the universe. These observations have revealed high values for the escape fraction of LyC photons, based on the observed ratio of ionizing to non-ionizing UV radiation. In particular, the LyC escape fractions for some of our Lyman continuum leaker candidates(LyCLCs) challenge models of stellar populations.

3.1 Introduction

Star-forming galaxies are expected to be responsible for the reionization of the intergalactic hydrogen at $z > 7$ (e.g., Robertson et al., 2015) and much of the ionizing background at $3 < z < 7$ (Nestor et al., 2013; Becker and Bolton, 2013; Becker et al., 2015). Therefore, there has been much interest in quantifying the fraction of ionizing photons that escapes from star-forming galaxies (the "escape fraction," f_{esc}).

Recent measurements of the UV luminosity functions of galaxies (e.g. Oesch et al., 2013; Alavi et al., 2014, 2016; Bouwens et al., 2015b; Atek et al., 2015) have shown that galaxies can provide enough ionizing photons by $z \sim 6$ if the luminosity function is extrapolated to luminosities beyond our current detection limits and if the escape fraction is high ($\sim$ 0.2 or more Bouwens et al., 2012; Robertson et al., 2013, 2015; Bouwens et al., 2015a). However, the escape fraction is not well constrained, nor is the mechanism allowing for leakage of ionizing (Lyman continuum, LyC) photons. Unfortunately direct detection of the ionizing photons from galaxies at the epoch of reionization or soon thereafter is not feasible due to the high opacity of the intergalactic medium (IGM) at $z \gtrsim 4$ (Fan et al., 2006; Prochaska et al., 2009). Hence, over the last two decades, many attempts have been made to detect escaping LyC from various types of star-forming galaxies at $z \lesssim 4$ (e.g. Leitherer et al., 1995; Steidel et al., 2001; Grimes et al., 2007, 2009; Siana et al., 2007, 2010, 2015; Cowie et al., 2009; Iwata et al.,

2009; Bridge et al., 2010; Vanzella et al., 2010; Boutsia et al., 2011; Nestor et al., 2011, 2013; Mostardi et al., 2013; Guaita et al., 2016).

At $z < 2$, despite higher IGM transmission and lower foreground contamination rates, only a handful of LyC emitters have been identified (Leitet et al., 2011, 2013; Borthakur et al., 2014; Izotov et al., 2016), with escape fractions less than 4% in all but one of the galaxies with a high leakage of $\sim 46\%$,(Izotov et al., 2018). At $2 < z < 4$, ground-based studies have yielded many LyC-emitting candidates. However, after careful re-examination of many of them with higher resolution HST images, only a few robust detections have been confirmed and all very recently (Vanzella et al., 2012, 2015; de Barros et al., 2016; Mostardi et al., 2015; Vanzella et al., 2016; Shapley et al., 2016; Bian et al., 2017).

Many indirect attempts also have been made to determine the Lyman continuum escape fraction (e.g. Heckman et al., 2011; Jones et al., 2013b; Borthakur et al., 2014; Alexandroff et al., 2015; Erb, 2015). Yet, we showed in previous chapter that these only provide the upper limits. we also discussed in chapter 1 that in order to minimize the foreground contamination and also to investigate the morphological signature of LyC probable escape mechanism we need to acquire high resolution space images of both the non ionizing and ionizing part of the spectra of candidate LyC leakers. In this chapter we follow up the target star-forming galaxies () previously investigated by Nestor et al. (2011, 2013) using the ground base narrow band imaging of SSA22 field with Keck and Subaro telescopes for which they also have acquired LRIS spectroscopy to find their redshift based on their Lyα emission line.

The present chapter is organized as follows: In Section 2, we describe the target galaxies and observational data. In Section 3, we present how the data reduction and preparation of final sample was conducted, and in Section 4 we present the results and discussion. Throughout the chapter, we adopt a cosmology with $\Omega_M = 0.3, \Omega_\Lambda = 0.7$

and $H_0 = 70$ km s^{-1} Mpc^{-1}. The flux densities are all in f_ν, i.e. are given in erg s^{-1} cm^{-2} Hz^{-1}, and the magnitudes are in the AB system.

3.2 Observational Data

3.2.1 Target Galaxies

We are following up the sample of 41 Lyman break galaxies (LBGs) and 91 Lyα emitters (LAEs) of Nestor et al. (2013) at z $>$ 3.055 in the SSA22a field. The details of how this target sample has been selected can be found in Nestor et al. (2011, 2013). In brief, it is using the deep multi-band imaging available in the SSA22a field which include ground-based broadband images in B, V, and R filter plus narrowband images with effective wavelengths at $\lambda \sim 3640$ Å and $\lambda \sim 4980$ Å (hereafter NB3640 and NB4980, respectively). The LyC region of our target galaxies at $z > 3.06$ was imaged with NB3640 filter with the Low Resolution Imaging Spectrograph (LRIS) on Keck I. The galaxies in the sample were selected by their Ly$_\alpha$ emission at z $>$ 3.09 with NB4980 filter or via a Lyman break selection using broadband filters (Steidel et al., 2003). Part of the NB4980 imaging was done also on LRIS/Keck I while the rest and all the broadband filter images were performed by Subaro Supreme Cam. These observations are summarized at Table 3.1 (borrowed from Nestor et al. (2011)).

For all of our sample galaxies the spectroscopic redshift was calculated using the blue arm of the LRIS dichroic spectrograph on Keck I (by probing Lyα) in ten slit masks with typical exposure times of 5400 s and photometric conditions with seeing ranging from 0.5″ to 0.7″.

Table 3.1: Description of Multi-band Ground-based Observations

Filter	Telescope/Instruments	Seeing/FWHM (″)	Exposure (s)
NB3640	Keck/LRIS-B	0.80	47636
NB4980	Keck/LRIS-R	0.80	33880
	Subaru/Suprime-Cam	0.76	25800
B	Subaru-Suprime-Cam	0.76	3927
V	Subaru-Suprime-Cam	0.60	3000
R	Subaru-Suprime-Cam	0.56	3000

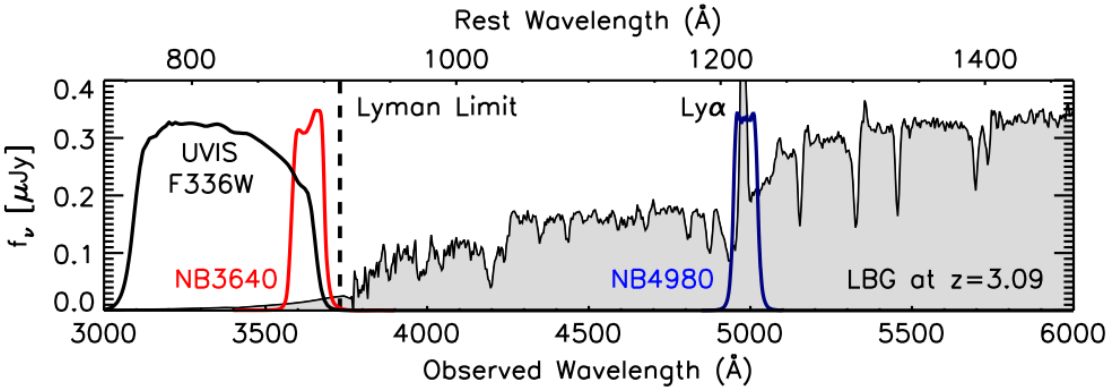

Figure 3.1: Shaded region shows the composite spectrum of Shapley et al. (2003) of $z \sim 3$ LBGs, shifted to the redshift of the overdensity in SSA22, z = 3.09. The spectrum below the Lyman limit is just an illustrative extrapolation assuming a constant f_ν corrected for the mean IGM transmission in $z = 3.09$ at each wavelength, i.e., $e^{(-\tau_{IGM})}$. Also plotted are the total system throughputs for the two WFC3/UVIS F336W and NB3640 filters, which samples the ionizing continua as well as that of NB4980 filter used to find Lyα emitters at the redshift of the over-density.

3.2.2 HST Observations

To make a clean sample of LyC leakers for which the possibility of foreground contamination is significantly reduced, and also to possibly detect the morphological signature of the LyC escape, we have to acquire high resolution Hubble images both in ionizing and non-ionizing regions of these galaxies. F336W filter on WFC3/UVIS probes the rest-frame LyC of galaxies at z $>$ 3.06 (see filter curve in Figure 3.1)

All of our target galaxies are spread in a single field of view of the Keck/LRIS ($5.5' \times 7.6'$) which is considerably larger than that of the HST WFC3/UVIS ($2.7' \times 2.7'$), and to detect the rest-frame LyC of these galaxies with HST very deep exposures are required. Previously Siana et al. (2015) has examined this field with one very deep pointing (hereafter P1) using F336W filter on WFC3/UVIS in cycle 17(PID: 11636, PI: Brian Siana) we extend that study by examining two more deep pointings (P2 and P3) in the same filter acquired in cycle 19 (PID: 12527, PI: Brian Siana).

For F336W images exposure times were long (half-orbit in length) to minimize the number of readouts. This is important as Below $\sim$ 4000 Å, read noise is the dominant source of noise in UVIS imaging. P1 is 32 orbit deep which is the deepest UV image taken yet and P2 and P3 are 12 orbits each. In each visit, a standard four-point dither (WFC3-UVIS- DITHER-BOX) was used (with a point spacing of $0.173''$) to achieve sub-pixel sampling of the PSF. Each visit performed the same dither pattern, but at slightly different central pointings spread over $\sim 3''$.

CTE degradation of the UVIS CCD detectors which is caused by radiation damage in the CCDs results in a loss of source flux and affects the photometry and morphology measurements especially in low background images (e.g., UV data; Teplitz et al. 2013). At Cycle 17 that UVIS was brand new CTE was not a problem. But in order to minimize the CTE issues for our F336W images in cycle 19 we applied post-flash of $8e^-$ pixel^{-1}

to our images. Though adding noise to already faint data seems strange, yet this has the effect of filling trapping sites, and hence preserving more of the electrons which might also comprise our precious LyC photons.

Note that in P3, which contains visits 4,5 and 6 of the PID the orientation of V4 is off by $\sim 30^{\circ}$ off from the other two. This I believe is due to some technical difficulties! Yet it can have an effect on source detection as CTE issues are more severe as we getaway from the readouts in the CCD chips, and having two different orientation in a same pointing might help to recover galaxies that might be lost in one orientation due to CTE degradation but not in the other.

In addition to the F336W images, we also obtained optical imaging in F814W with the Wide Field Camera on the Advanced Camera for Surveys (ACS/WFC) which probe the non-ionizing rest-frame UV continuum of the targets. These images are both from aforementioned PIDs and the Archival data from a three-orbit image from a Cycle 13 program (PID 10405, PI: Scott Chapman) and a deep Cycle 11 program (PID 9760, PI: Roberto Abraham).

Table 3.2 summarizes the HST data, used in this study. You can also find the coverage footprint in F366W filter in Figure 3.2 which covers almost half of the area of where the target galaxies are and also the coverage footprint in F814W filter in Figure 3.3 which covers $\sim$ 90% of the target field. Though as the F336W were selected so that to contain most of the LAEs and LBGs in our initial sample, $\sim$ 70% of our target sample have coverage in both filters.

3.2.3 MOSFIRE spectra

Near-IR spectra were obtained by Charles Steidel for four of our targets using the MOSFIRE instrument on the Keck I telescope. With 3 night K-band observation and

Table 3.2: HST Observations

Filter		PI	Cycle	PID#	Expusure Time s
F336W	P_1	Siana	17	11636	64×1325
	P_2	Siana	19	12527	24×1270
	P_3	Siana	19	12527	24 × 1270
F814W		Siana	17	11636	2280
		Siana	19	12527	6864
		Chapman	15	10405	18432
		Abraham	13	9760	72150

one night H-band Observation for C14,M2 and M5 (September 2012). And 1 K-band spectra also for C083. The exposure time for each K-band spectra is 30 × 178.93 s, and for H-band the exposure time is 30 × 120 s. Hence The total exposure times for C14, M2 and M5 is $\sim$ 4.5 hours in K-band and 1 hour in H-band while for C083 we only have a 90 minute exposure in K-band. Though the conditions were photometric for the observing nights with seeing $\sim 0.5'' - 0.7''$, none of the galaxies showed any emission line in their spectra. The absence of expected O$[III]$ and H_β in K-band spectra and O$[II]$ in H-band spectra despite the deep and good quality weather is somehow puzzling.

3.3 Data Reduction and Analysis

For our F814W image as the Background level in NIR is high so that while read out the CCD's traps gets filled and also the non-ionizing flux of our targets are well above the background so neither the CTE nor the structures within dark images are not concerning. Yet to prepare their mosaics, we first CTE-corrected and dark-subtracted all of the flat- fielded images using the PYRAF/ STSDAS CALACS and CALWF3 programs, respectively. Then the calibrated images were aligned in each individual visits using

the Tweakreg (Gonzaga et al. 2012) tasks in the PYRAF/DrizzlePac package and thier WCS was updated.

In F336W filter, though we used post flash of 8 electron per pixel which will considerably reduce the CTE degradation issue (Teplitz et al., 2013), still the background from sky, read-noise, and post-flash are very low that we need a very careful subtraction of the dark images as well as correction for charge loss in both our UV and dark images. The traditional standard dark subtraction was not adequate in removing dark structures and hot pixels and leaves a background gradient and blotchy patterns in the final science image. So we did the same improved dark subtraction and hot pixel removal technique as explained in detail in Section 2.3.2 for our UV images (Rafelski et al., 2015; Vasei et al., 2016) a detailed description of this technique can be found in (Rafelski et al., 2015; Vasei et al., 2016). To correct for these charge losses in our UV images, we also used a pixel-based CTE correction tool provided on the STScI website.

The standard calibrations like F814W images was performed afterward and the calibrated images then were aligned together in each individual pointing (24 or 64 images based on the pointing) using the Tweakreg (Gonzaga et al., 2012) tasks in the and their WCS was updated.

As our aim is to obtain High resolution of the target galaxies that have been cataloged based on the Suabro/Supreme Cam wild filter images, we need to align our images based on our catalogue. In order to do that we take R-band Subaro image which has the closest wavelength range to the F814W image as the reference image. Subaro and HST are using two different WCS systems and AstroDrizzle could not align the two images directly together. Hence we run the Source Extractor software version 2.19.5 (SExtractor; Bertin Arnouts 1996) to make a catalogue of R-band and use this catalogue to astrometricaly align and combine the HST F814W images with this reference catalog using the Tweakreg and AstroDrizzle (Gonzaga et al., 2012) tasks in

the PYRAF/DrizzlePac package, respectively. The AstroDrizzle program subtracts the background, rejects the cosmic rays, and corrects the input images for the geometric distortion due to the non-linear mapping of the sky onto the detector. In addition to the science output images, AstroDrizzle generates an inverse variance map (IVM) which we use later to make the weight images and to calculate the image depths.

As the pixel scale of the ACS/F814W images of 0.05″ is larger than that of the UVIS F336W images (0.04″) and our slitter pattern has allowed for sub-pixel PSF, we chose 40 mas as the pixel scale for all of our large mosaic files. These images are $6.83' \times 9.07'$ to also include some regions off the LRIS coverage that we had HST coverage as well for further spectroscopy follow ups.

We used these large mosaic file in F814W to align and combine the UV images in to a same Large Mosaic image with the same pixel scale by AstroDrizzle. The final alignments between the ground base observations and HST observation is better than 80mas (0.2 of the mosaics pixel scale). These large mosaic files are shown in Figure 3.2 and 3.3.

3.3.1 Object Detection and Photometry

We use the Source Extractor software version 2.19.5 (SExtractor; Bertin Arnouts 1996) for object detection and photometry. SExtractor is used in dual image mode, where objects are detected in the F814W (rest-frame non-ioizing UV for our target galaxies) mosaic, and the photometry is measured on all mosaics for each filter. In this way, fluxes of sources are measured using the same isophotal apertures, and fluxes are measured for all objects regardless of any flux decrement in the NUV mosaics due to the Lyman limit.

We also used the inverse variance map (IVM) generated by AstroDrizzle program

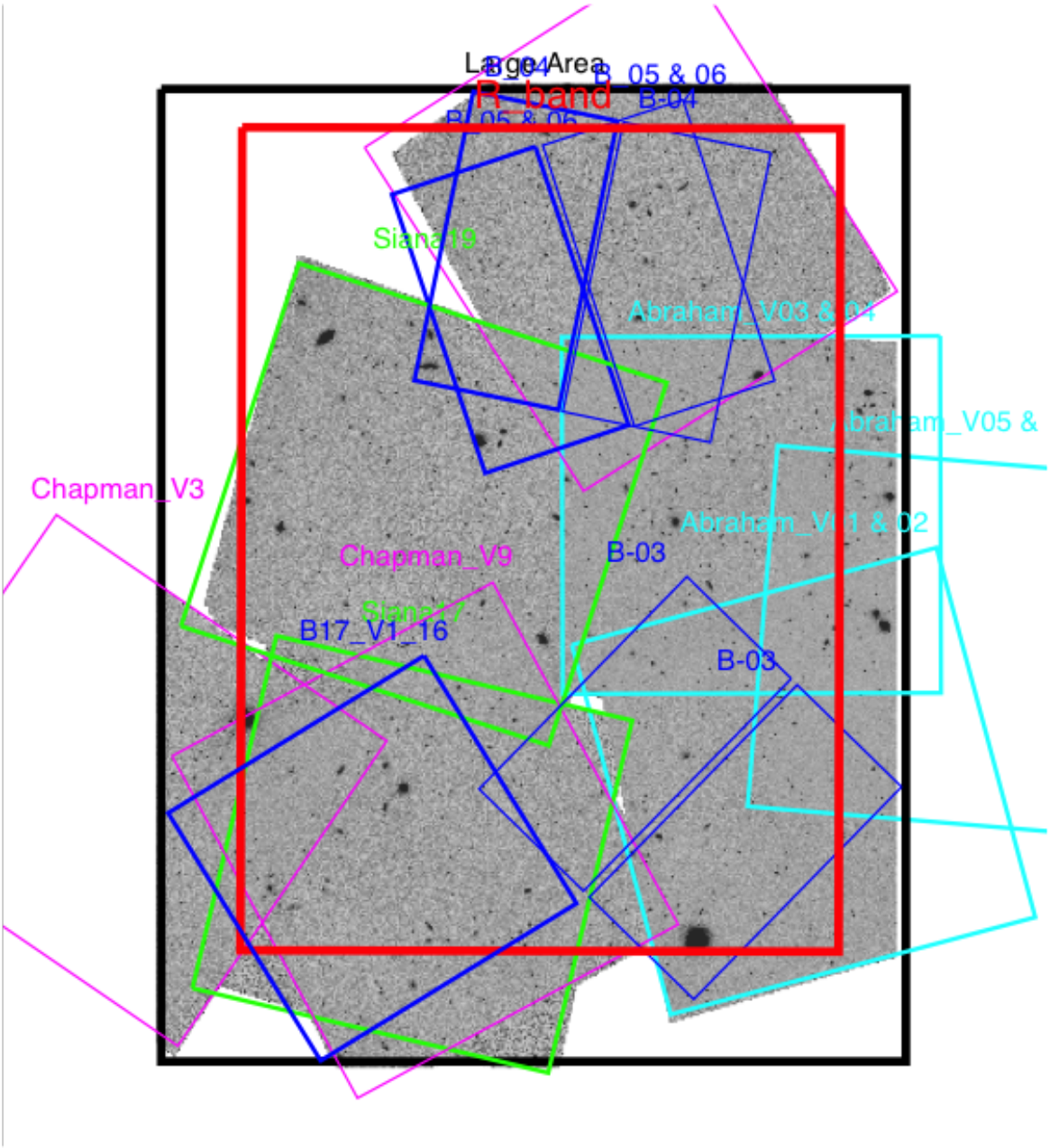

Figure 3.2: The Coverage of the F814W around the target field depicted by red rectangle, the F814W mosaic image covers ∼ 90% of the target field of view. The HST mosaic image is shown by black rectangle. Also shown is: The F336W pointings in blue; and F814W images of Siana, Chapman, and Abraham in green, magenta, and cyan, respectively.

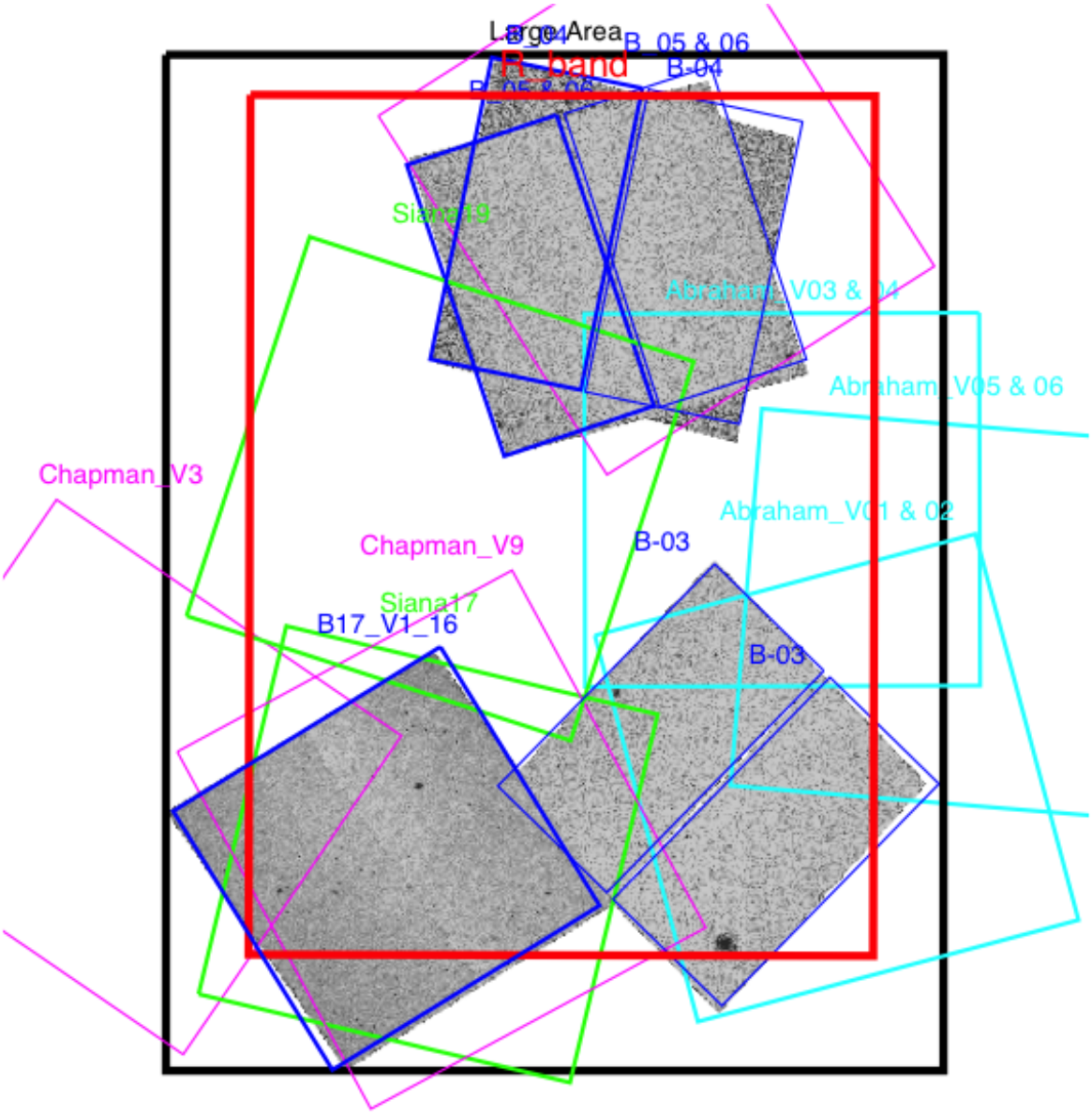

Figure 3.3: The Coverage of the F336W around the target field depicted by red rectangle, the F336W mosaic image covers $\sim$ 50% of the target field of view. The HST mosaic image is shown by black rectangle. Also shown is: The F336W pointings in blue; and F814W images of Siana, Chapman, and Abraham in green, magenta, and cyan, respectively.

to construct the rms weight map images by taking their inverse square root. SExtractor uses these rms MAPs to derive the flux uncertainties. We correct these rms MAPs for the correlated noise (Casertano et al., 2000) from drizzling the mosaics. Finally, we correct our photometry for the Galactic extinction toward each cluster using the Schlafly and Finkbeiner (2011) IR dust maps. Though, as the exposure times vary greatly in our mosaic images, the background and hence the flux errors can vary wildly through the image.

We examined two sets of apertures in our F814W mosaic image. first above 1.5 σ above the local background, second apertures above a fixed threshold values (look up the value from Sextractor config file). This was intended to work similar to the strategy of running Sextractor in hot and cold modes, but as all of our target galaxies are expected to be much brighter in non-ionizing image than in ionizing image, we expect to get high signal to noise for them in F814W and the central part of the galaxies will be in the apertures anyway (it is not like we are finding new sources of interest). Though at places with higher noise(less exposure time or at edges of each visits) we will lose the outskirt of our galaxies and as we use that same aperture to detect LyC in F336W we might lose the LyC leakages that are in the outskirts of our galaxies. This diffused LyC leakage might be due to runaway stars or interactions between galaxies. Hence for the next section we only used the latter apertures which are above the fixed threshold in F814W.

3.4 Results

First step is to cross-match our target catalogue and our HST catalogue to find our 91 galaxies that have the following conditions:

1. Have confirmed z $>$ 3.06 .
2. Are covered in both of the HST mosaic images.
3. The separation angle between their spacial place in the catalog and HST images are less than $1''$.

The last condition is to make sure we have measured the redshift for the right galaxy and the flux in F336 is indeed LyC. Though we examined all the remaining candidates later for the possibility of false identification.

3.4.1 Identifying Lyman Continuum Leaker Candidates (LyCLC)

In the next step we examined every object in our catalogue for which we have $\sim 3\sigma$ or more detection in the Lyman continuum F336W filter. This left us with 17 candidates, for which we closely looked for the separation angel between the two catalogs and to make sure we have obtained the redshift for the component with the LyC leakage. We then omitted the contaminated sources found by Siana et al. (2015) and Nestor et al. (2013), also three sources that the two catalogs have selected two separate galaxies and a know AGN from our sample as well as the sources for which the aperture in the F336W image was so close to the edge of the frame that the signal to noise was not reliable, we found 5 final sources for our Lyman continuum leaker candidates. They are C074 and C083 from LAE catalog of Nestor et. al. 2013, and C14, M2 and M5 from their LBG sample.

Before we discuss each of these final candidates, we summarize the analysis we done on all or part of them.

3.4.2 IGM Transmission

To estimate the average transmission of the IGM, we used the same technique as in chapter 2. We ran a Monte Carlo simulation (see Siana et al., 2007, for details) using the known distributions of HI absorber column densities as a function of redshift (Janknecht et al., 2006; Rao et al., 2006; Ribaudo et al., 2011; O'Meara et al., 2013) as summarized in Table 2 of Alavi et al. (2014). We simulate 1000 LOSs through the IGM to the redshift of each of our final galaxies measured based on their Lyα emission from LRIS spectra. Each LOS gives the transmission as a function of wavelength, from which we determine average transmission through the F336W filter for each galaxy.

$$e^{-\tau_{H_{I,IGM}}} = \frac{\int e^{-\tau_\lambda} T_\lambda d\lambda}{\int T_\lambda d\lambda} \tag{3.1}$$

Where the IGM opacity (τ) and the filter transmission(T) are both function of wavelength. The average transmission for each galaxy through the IGM is represented in Table 3.3. The value for the average IGM transmission through the F336W filter curve at z = 3.066 and z=3.385 was estimated to be 0.27 and 0.1 respectively. Though the value can vary wildly among sight lines as is shown in the Figure 3.4.

3.4.3 Relative Escape Fractions

After calculating the average transmission for the redshift of each galaxy, the relative escape fraction, $f_{esc,rel}$, can be assessed as described in section 2.2, based on eq. 2.2:

$$f_{esc,rel} = \frac{\left(F_{1500}/F_{LyC}\right)_{stel}}{\left(F_{1500}/F_{LyC}\right)_{obs}} \times e^{\tau_{H_{I,IGM}}} \tag{3.2}$$

Where F_{1500} and F_{LyC} are the flux densities in f_ν at 1500Å (in F814W) and in the LyC (F336W fluxes,). To use this relation, there are two further points we need

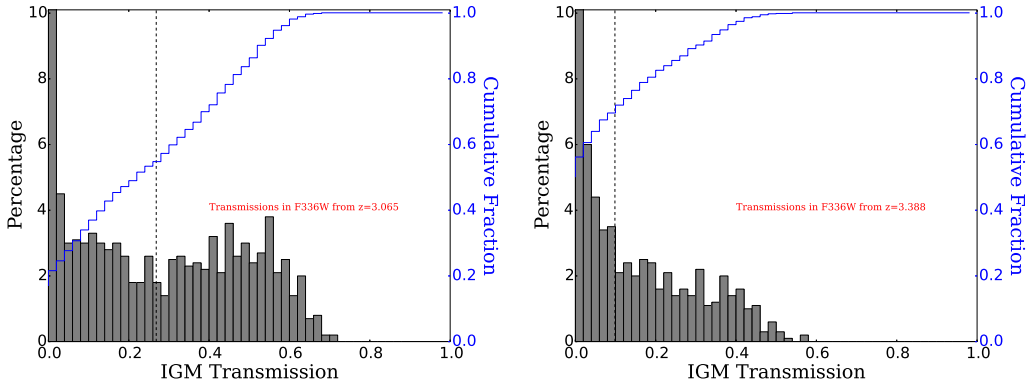

Figure 3.4: Left: A histogram of the F336W filter transmission-weighted IGM transmission of the 1000 simulated LOS. The vertical dashed line shows the average transmission (0.27) through the filter and the blue line shows the cumulative fraction up to any given IGM transmission. Right: The same histogram for our simulation at z=3.39. The vertical dashed line shows the same average transmission (0.1) through the filter and the blue line shows the cumulative fraction up to any given IGM transmission. We note that increasingly higher number of the LOS have low transmission(the vertical line is cut at 10 percent to better show the rest of the distribution.

to address. First the LyC flux density before IGM attenuation is assumed to be flat (constant in f_ν), and second intrinsic value for the amplitude of the Lyman break in the stellar SED is assumed to be

The reason for the first assumption is that the ACS/F814W filter has a pivot wavelength at $\sim 1850 - 2000$ Å for the range of our galaxy redshifts. and we need the fluxes to be measured in exactly the same apertures to get the flux ratios. The lack of full coverage of UVIS F625W that detect $\sim$ 1500 Å for our sample galaxies, led us to use F814W instead. Though with one UVIS pointing (PID:12943 ; PI: Yujin Yang) we have F625W fluxes measured for three of our final candidates (C14, C074, C083).

Also for the second assumption of fixed stellar flux density ratio we note that it can be affected by short term variations in the star formation history such as a burst of star formation or a sudden decrease of it. This is because the LyC production will be affected in a much smaller time scales than that of the 1500 Å continuum (Domínguez et al.,

2015). Also when effects of the binarity and rotation of massive stars are included this ratio can significantly be reduced as their main-sequence lifetime and effective temperature would increase (Eldridge and Stanway, 2009).

despite all these uncertainties, Eq. 3.2 is useful as it does not require knowledge of dust attenuation and the 1500Å flux density of high redshift galaxies can be easily measured.

3.4.4 Characteristics of LyCLC

Because there are only five galaxies in our sample and each has different properties, we have chosen to discuss the objects individually. The properties of these galaxies are summarized in Table 3.3 and their spatial distribution also is presented at figure 3.10.

C14

C14 was initially in the LBG samples as its redshift is higher than that to be detected with the NB4980 as a LAE. Though there is a faint component near it but the Lyα appears to be coming from the bright component for which we also have LyC detection. Though the O$[III]$ flux was expected to be detected in MOSFIRE spectra, it is not there. Yet as no other emission lines were observed in either of the spectra which makes the probability of a foreground contamination slim as well. We also have detected it in our UVIS/F625W filter with an AB magnitude of 25.77 which if used instead of $m_{F814W} = 25.47$ will reduce the relative escape fraction measured in Table 3.3 to 5.51. Though this escape fraction is still high we retain C14 as a very likely LyCLC.

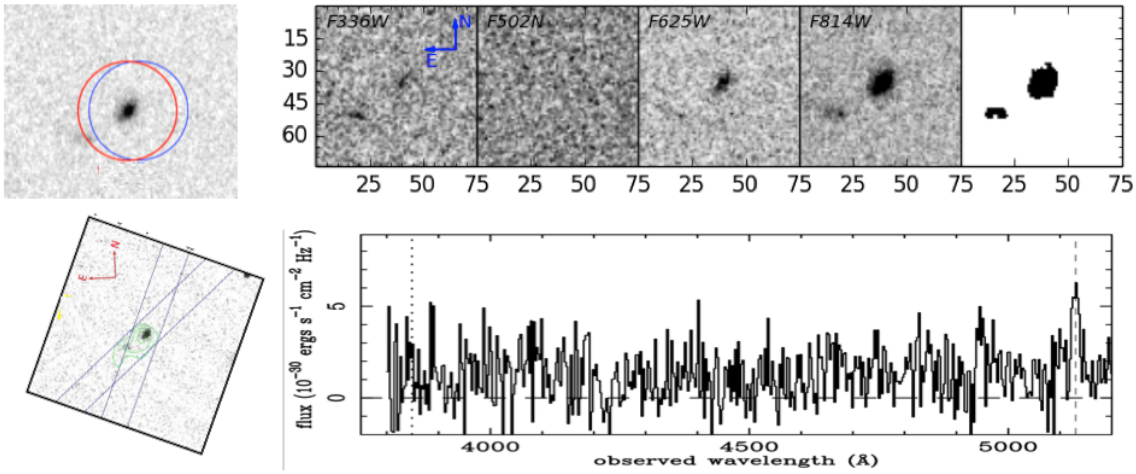

Figure 3.5: Top right: C14 in the detection F814W image with red and blue circle showing its location in HST and ground catalog respectively. Top left: The aperture and the HST images are shown. Bottom right: the position of the two orientation for LRIS slits, though the spectra containing the two object was noisy and was not used. Bottom left: LRIS spectra that shows the Lyα

.

C074

C074 is one of the initial LAE samples with a redshift very close to the ideal redshift for F336W to detect its Lyman Continuum. Unfortunately we don't have MOSFIRE data for this galaxy to inspect foreground contamination for this galaxy. Also the Lyα is not there in the deep slit orientation of the LRIS spectra (though it partly samples the Lyα contour in Figure 3.6). The Lyα $_{EW}$ is also small for this galaxy (5.87 Å in rest-frame). We also have detected it in our UVIS/F625W filter with an AB magnitude of 26.40 which if used instead of $m_{F814W} = 26.38$ will only reduce the measured escape faction to 17.64. This is a very high value especially as at this z the average IGM transmission we derived can't be increased by more than a factor of 3. Also this is the only candidates that our preliminary SED doesn't indicated a Lyman decrement. And close look at F814W image shows an extended galaxy with low surface brightness on top of the

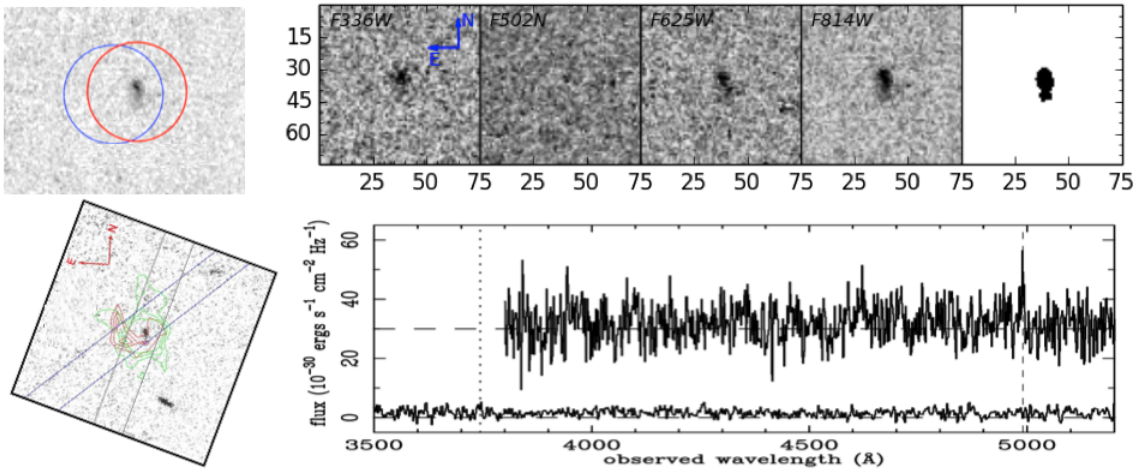

Figure 3.6: Top right: C074 in the detection F814W image with red and blue circle showing its location in HST and ground catalog respectively. Top left: The aperture and the HST images are shown. Bottom right: the position of the two orientation for LRIS slits, though the deep spectra does not show the Lyα line, so the constraints on this target is weak. Bottom left: LRIS spectra that shows the Lyα

location of this candidate. Hence we conclude this candidate to be contaminated and removed it from our calculations in the stacked sample.

C083

C083 is also one of the initial LAE samples with a redshift ideal for F336W to detect its LyC (Just blue ward of the Lyman limit). Unfortunately we have only one shallow MOSFIRE data in K-band (1.5 hr) for this rather faint galaxy and it doesn't show any sign of emission lines, so a strong foreground contaminating galaxies are less likely. Also the double peaked Lyα line insures the redshift is accurately measured and the other component which also was detected in F336W was not located in LRIS slit. We also have detected C083 in our UVIS/F625W filter with an AB magnitude of 27.46 which if used instead of $m_{F814W} = 27.07$ will reduce the relative escape fraction measured in Table 3.3, to 1.15. This gives the most normal case for our LyCLCs. And we

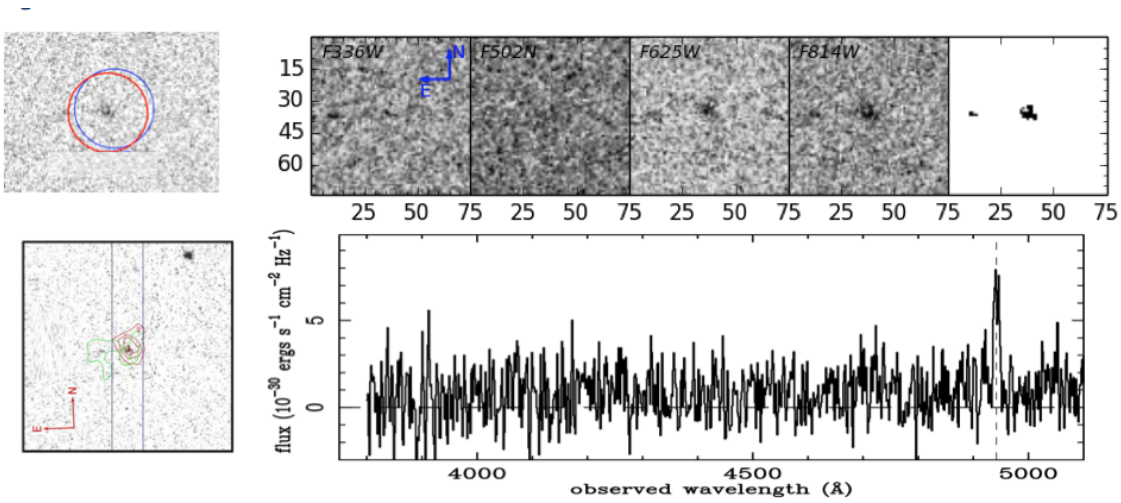

Figure 3.7: Top right: C083 in the detection F814W image with red and blue circle showing its location in HST and ground catalog respectively. Top left: The aperture and the HST images are shown. Bottom right: the position of the shallow-mask LRIS slit. Bottom left: LRIS spectra that shows the Lyα at $\lambda = 4942$ ÅṄo other line was detected.

are almost certain that this is actually a LyCL.

M5

M5 was also initially in the LBG samples as its redshift is higher than that to be detected with the NB4980 as a LAE. There is also a faint component near it westward(M5W). Also Lyα is appear in both the deep and shallow orientations at $\sim$ 5260Å and is most likely coming from the bright component (M5E), Nestor et. al. 2013 detected a foreground contamination emission line at $\sim$ 4040Å in the deep slit for which we also have LyC detection. Though the O[III] flux was expected to be detected in MOSFIRE spectra, it is not there. yet as no other emission lines were observed in either and both of the clumps are observed in the F336W one of them at least is most likely an uncontaminated LYCLC. But it requires further examination of each component to determine the right candidate. More over lack of coverage in F625W is not let us correct for any

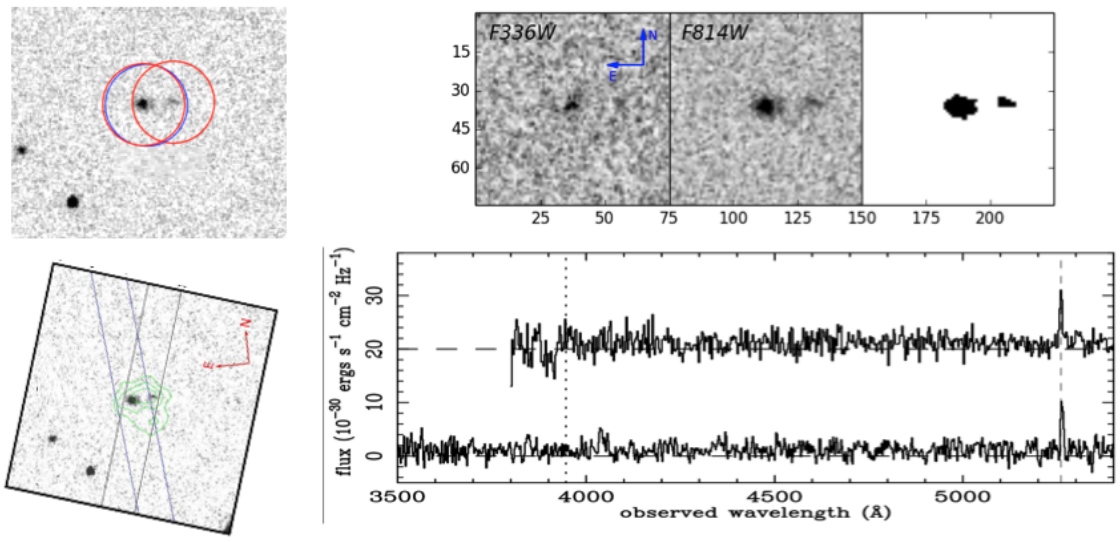

Figure 3.8: Top right: M5E and M5W in the detection F814W image with red circles and with blue circle showing its location in ground catalog. Top left: The isophot aperture and the HST images are shown. Bottom right: the position of the two orientation for LRIS slits, red for deep and blue for shallow exposures. Bottom left: LRIS spectra that shows the Lyα at $\sim$ 5260ÅṪhe deep spectra containing the two object is showing a lower redshift contamination emission line at $\sim$ 4040Å.

possible un-flat UV slope in f_ν(or $\beta \neq -2$).

M2

M2 was also initially in the LBG samples as its redshift is higher than that to be detected with the NB4980 as a LAE. There is also a faint component near it toward south east just outside the 1″ circle. Also Lyα is appear in both of its shallow orientations at $\sim$ 5334Å as not any foreground contamination emission line was detected in any of the LRIS or MOSFIRE spectra. Though also there is no F625W flux measurement is available to correct for its rather high estimated $f_{esc,rel}$ yet the high redshift and hence low average IGM transmission used aloow for up to a factor of 6 correction if the LOS is cleared out by the foreground over-density of SSA22A field.

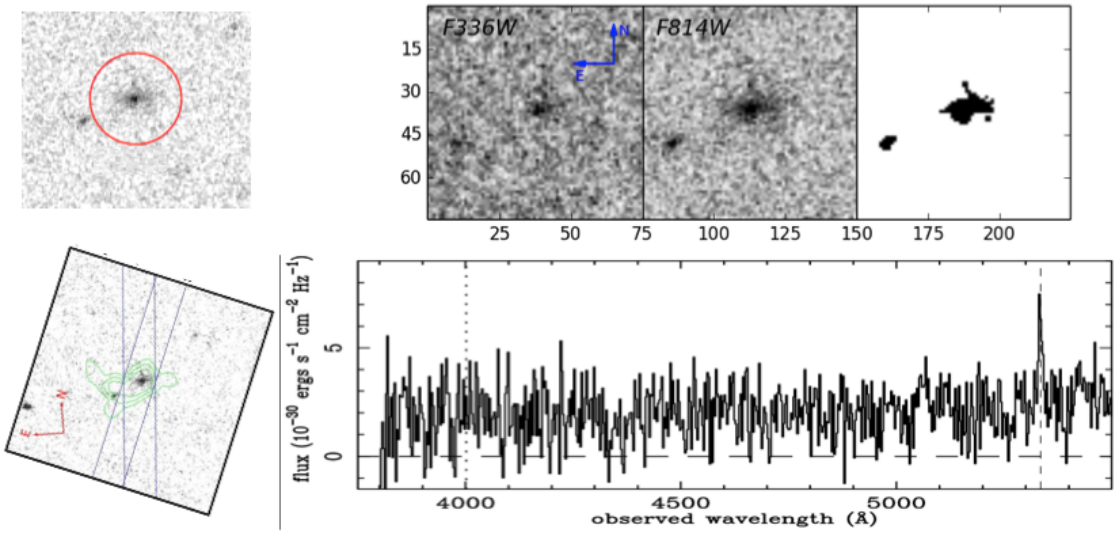

Figure 3.9: Top right: Showing the astrometrical location of M2 in the detection F814W image with red and showing its location in ground catalog with blue circle respectively, here they are exactly on top of each other showing almost zero separation angle. Top left: The isophot aperture and the HST images are shown. Bottom right: the position of the two orientation for LRIS slits with shallow exposures. Bottom left: LRIS spectra that shows the Lyα at $\lambda \sim 5334$Å.

Figure 3.9: Top right: Showing the astrometrical location of M2 in the detection F814W image with red

Table 3.3: The Properties of our Final LyC Emitter Candidates

Name	ID	RA[a]	Dec[a]	z [b]	M814	R	M336	NB3640	$e^{-\tau_{IGM}}$ [c]	$f^{d}_{esc,rel}$	$Ly\alpha^{e}_{EW}$	OIII Flux[f]
		°	°								Å	10^{-30} erg s^{-1} cm^{-2} Hz^{-1}
C074	laec3_1321a	334.4020	0.2152	3.100	26.38	26.16	26.89	25.52	0.248	17.97	24.07	0.48
C14	C14	334.3919	0.2142	3.216	25.47	25.28	27.43	26.43	0.161	7.28	54.21	1.11
C083	laec3_0754	334.3687	0.2022	3.066	27.07	26.46	28.64	26.84	0.269	6.24	15.46	0.25
M5	M5E	334.3588	0.1924	3.324	25.87	25.30	27.58	26.31	0.130	11.35	62.26	0.77
M5	M5W	334.3586	0.1924	3.3!?	27.83	- - -	29.18	- - -	0.130	15.81	- - -	0.13
M2	M2	334.3899	0.1862	3.385	25.88	25.28	27.41	25.99	0.099	17.59	18.33	0.76

a Based on HST locations.
b From LRIS Ly$_\alpha$ line.
c The average value based on our explained montecarlo simulation for the redshift of each galaxy.
d UsingF814W with no correction here for the non-ionizing flux density.
e Based on calculation explained in the text(convert to rest-frame).
f An estimatation of the expected flux density in units of 10^{-30} erg s^{-1} cm^{-2} Hz^{-1} based on the conversion from Ly$_\alpha$ Flux as explained in the text.

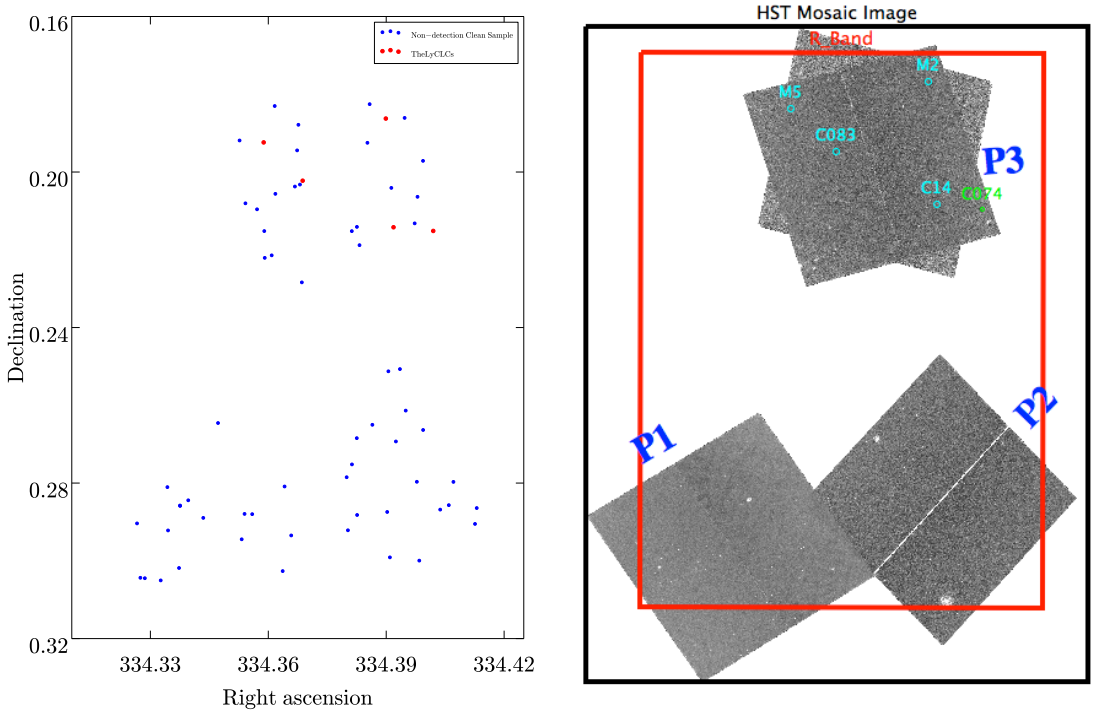

Figure 3.10: The location of all of our final clean samples including both the LyCLCs(all five included) shown in red and the ones with non-detection(61 targets)shown in blue. It is Curious to note that all of our leakers are in a single pointing (P3).

3.4.5 Analyzing the Stacked Sample

After removing the contaminated samples in the detected LyC leakers we reviewed the postage stamps of all the rest of the objects and removed the ones where there were multiple sources with the spatial position of the ground data was on top of one of the clumps that is not detected in the F336W image. in this way we build a clean sample of 61 sources without detection. Their spatial distribution is shown in Figure 3.10.

We stacked the samples once including and once without including the LyCLCs to find the average value of relative escape fraction for our final clean sample. For this purpose we used merely flux ratio of the stacked spectral flux densities in F814W and F336W filters, and using the mean redshift of 3.1 to calculate the average IGM transmission. The upper limits we get for the escape fractions are 0.11 and 0.08 when

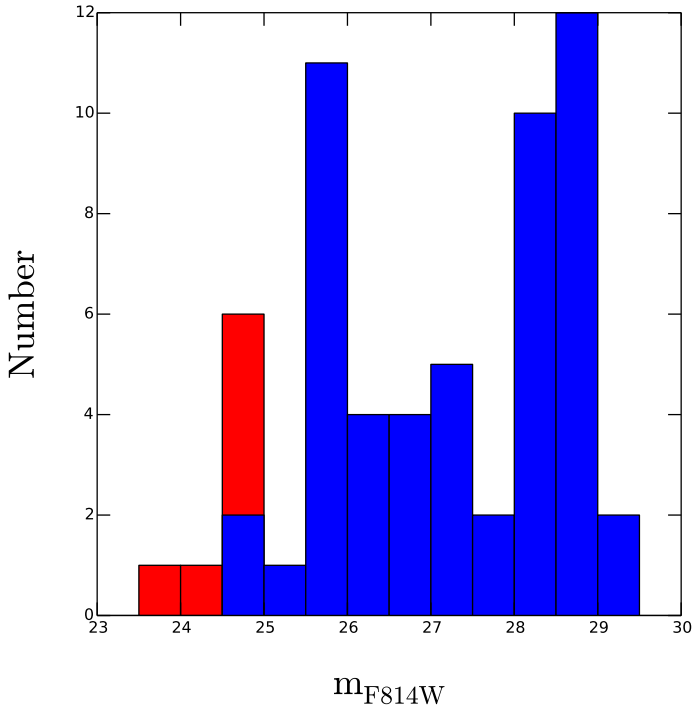

Figure 3.11: UV magnitude histograms in F814W filter for our 61 non detections sample. They have been divided to two sub-samples of Luminous versus faint so that they have roughly the same flux density in the F814W filter. This was done to see if there is any correlation between the luminosity and $f_{esc,rel}$.

we included or excluded the 4 LyCLCs, respectively.

Also for our non-detection sample we divide them into two samples of luminous versus faint so that the sum of the fluxes in F814W be roughly the same for the two subsample. The cutoff value for the two sample was at $m_{F814W} = 24.7$ with the luminous subsample containing only 8 galaxies and the other 53 were in the faint sample. The distribution of their magnitude are given in Figure 3.11. Based on their observed spectral flux density ratios in the F814w and F336W, we estimated an upper limit of 0.09 and 0.07 for our faint and luminous subsamples respectively. As these are only upper limits as no signal was detected, we cannot conclude that necessarily fainter galaxies have higher average escape fraction.

3.5 Discussion and Conclusion

There are a few points that rises from our results that needs to be discussed here. First we have to address the high relative escape fractions for our candidates and their implications, second to determine the expected rate of our contamination as all of the candidates in the deep pointing (P1) inspected by Siana et al. (2015) was determined to be contamination. Third, we notice that all of our LyCLCs are located in a single pointing (P3) in our cycle 19, we discuss the possible causes for this.

3.5.1 Implications of High Values of $f_{esc,rel}$ in our LyCLCs

We know that physically it is impossible for absolute escape fraction, $f_{esc,abs}$, to be higher that unity in any sight line. Though the relation between the two as mentioned in Eq. 2.1 is:

$$f_{esc,abs} = f_{esc,rel} 10^{-0.4 A_{1500}} \tag{3.3}$$

Where A_{1500} is the dust attenuation, in magnitudes, at 1500 Å . For a Calzetti reddening law (Calzetti, 1997) we would have $A_{1500} = 10.33E(B-V)$. For our LyCLCs (Lyman Continuum Leaker Candidates) where we didn't have F625W filter to correct for the difference in flux density at rest-frame $\sim$ 2000Å from F814W to $\sim$ 1500 Å we even have to correct for a higher dust attenuation values of A_{2000}. And hence absolute escape fraction is always smaller than the relative escape fraction. like, in the case of cosmic Horseshoe it four times smaller. Though the greater the escape fraction is the less material is on the line of sight and less dust extinction will be there.

Though the main cause of our high values for $f_{esc,rel}$ might be an exceptionally clear LoS with high transmission. In our calculations for each redshift we used average

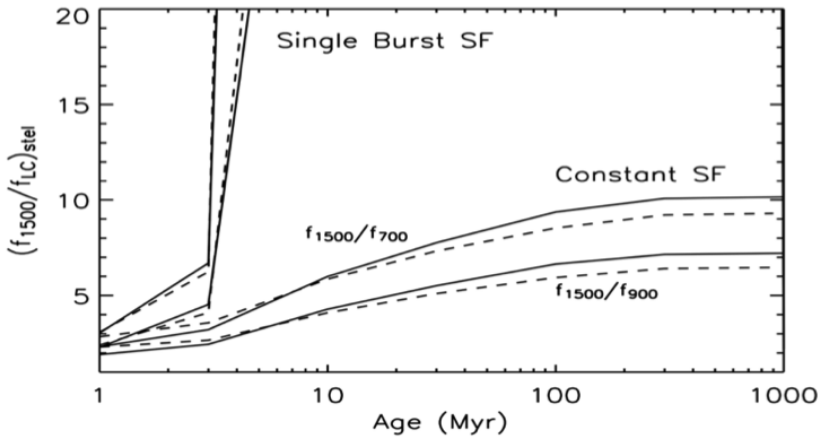

Figure 3.12: From Siana et al. (2007); The f_{1500}/f_{700} and f_{1500}/f_{900} intrinsic flux ratios as a function of time since onset of star formation using the BC03 (solid lines) and Starburst99 (dashed lines) models.

simulated transmission values, yet as is indicated by Figure 3.4 there is possibility that a LoS have a higher transmission by a factor of ~ 3 to 6 depending on the redshift. we will discuss this possibility next.

The other main factor in our calculation is the adopted intrinsic(stellar) flux density ratios of 6, which was based on the simulation using stellar population synthesis models from both Bruzual Charlot (2003) and Leitherer et al. (1999) and is depicted in Siana et al. (2007, their Figure 1) shown here in Figure 3.12. It is shown that a recent episode of star formation can reduce the $(f_{1500}/f_{900})_{stel}$ by at least a factor of 2 or 3 from our adapted value of 6. And of course our sample of Lyman Continuum detected galaxies are biased to containing this galaxies with higher LyC production rates even if it is only a short term variation see also (Domuez et al. 2014). also the other factor is that these models do not account for the effects of binarity and rotation of massive stars which in turn can prolong their main-sequence lifetime and increase their effective temperature and lead to higher value of Lyman Continuum flux density and lower our ratio by another factor of ~ 2 (Eldridge and Stanway, 2009).

Accounting for all these effect all of our final four candidates can have actually a less than unity escape fraction, and be real detection. the other option is that we have some contamination in them as well so we have to account for the rate of contamination in our sample as well.

3.5.2 The Probability of Contaminations in Our Sample

There have been two other studies for LyC emitters at this redshift on SSA22 filed, one detecting no LyC emitters (Siana et al., 2015), while the other (Fletcher et al., 2018) claiming multiple detections in another location of SSA22 field. It can be confusing to synthesize these into a unifying picture. It is critical to carefully consider contamination and its effects on each survey when trying to compare results.

Though the rate of contamination from foreground galaxies is quite low at these wavelengths. As an example, the odds of a foreground galaxy with $U_{AB} \leq 27.5$ lying within $1''.0$ of a target galaxy at $z \sim 3$ is roughly 8.5% given the completeness corrected surface density tabulated in Vanzella et al. (2010) and taken from Nonino et al. (2009). But detection of LyC emitters is also rare. Obviously, if the detection rate is near the contamination rate, then most or all of the candidate LyC emitters will be spurious.

Our four final candidates range in m_{F336W} from 26.84 to 27.58 (29.18 for our less likely candidate of $M5_W$). We followed the method explained and used on our initial data by Nestor et.al. (2013, look at their section 5.1) and corrected it for our image depth and better spatial resolution of HST to obtain a 6.2% chance of contamination for our galaxies which is in agreement with the value reported in Vanzella et al. (2010).

Initially we had 91 target galaxies matched with HST images, yet we have excluded 18 of them (6 in our detected samples and 12 in our non detection sample) based on noisy data near the edge or the ones that we had calculated the redshift for a com-

ponent not associated with the LyC detection. This leave us with 73 sample galaxies and our expected contaminated galaxies based on our simulated contamination rate of 6.2% would be 4.5 galaxies in our sample.

Among these 73 galaxies, we already have eliminated 6 galaxies due to contamination based on their LRIS or NIRSPEC spectra (and are reported in Siana et. al. (2015) and Nestor et. al. (2013)). We also have excluded C74 as a foreground contaminated galaxy in our initial sample. So we claim that the four LyCLCs reported here, have a good chance to be actual LyC detections.

3.5.3 On the Spatial Distribution of our LyCLCs

The fact that all of our four final LyCLCs are in a same pointing and can be fitted in an aperture with a radius of $72''$ of each other while the rest of the field haven't produced a single Lyc emitter candidate is interesting and worth noting. First we notice that in P3, which contains visits 4,5 and 6 of the cycle19 observations, the orientation of V4 is off by $\sim 30^{\circ}$ off from the other two. For whatever reason this has happened, it might have an effect on source detection by reducing the average effect of CTE on the objects. CTE issues are more severe as we getaway from the readouts in the CCD chips, and having two different orientation in a same pointing might help to recover galaxies that might be lost in one orientation due to CTE degradation but not in the other. If this was the case it can be tested in future observations easily. The other factor might be due to cosmic variance, and the fact that we know sight lines parallel to each other with small angular separation are coherence. (e.g. Becker et al., 2004, where they studied the spatial coherence of the intergalactic medium toward two pairs of high-redshift quasars). Though the proper distance between the two furthest galaxies in our LyCLCs are about 1.1 Mpc, an extreme over density like ssa22 is expected to create

voids around itself, where due to under density the rate of recombination is small and we expect a completely ionized IGM at z$\sim$ 3. It might be the structure of the cosmic web is such that for this pointing our candidates (3 of them far behind the SSA22 over density) might have a LOS with an extremely high transmission. This also will agree with the high relative escape fraction we measure for these galaxies.

References

Alavi, A., Siana, B., Richard, J., Rafelski, M., Jauzac, M., Limousin, M., Freeman, W. R., Scarlata, C., Robertson, B., Stark, D. P., Teplitz, H. I., and Desai, V.: 2016, *ApJ* **832**, 56

Alavi, A., Siana, B., Richard, J., Stark, D. P., Scarlata, C., Teplitz, H. I., Freeman, W. R., Dominguez, A., Rafelski, M., Robertson, B., and Kewley, L.: 2014, *ApJ* **780**, 143

Alexandroff, R., Heckman, T., Borthakur, S., Overzier, R., and Leitherer, C.: 2015, *ArXiv e-prints*

Atek, H., Richard, J., Jauzac, M., Kneib, J.-P., Natarajan, P., Limousin, M., Schaerer, D., Jullo, E., Ebeling, H., Egami, E., and Clement, B.: 2015, *ApJ* **814**, 69

Becker, G. D. and Bolton, J. S.: 2013, *MNRAS* **436**, 1023

Becker, G. D., Sargent, W. L. W., and Rauch, M.: 2004, *ApJ* **613**, 61

Becker, R., Bianchini, L., Dissertori, G., Djambazov, L., Donega, M., Lustermann, W., Marini, A. C., Nessi-Tedaldi, F., Pandolfi, F., Peruzzi, M., Schönenberger, M., Cavallari, F., Dafinei, I., Diemoz, M., Lope, C. J., Meridiani, P., Nuccetelli, M., Paramatti, R., Pellegrino, F., Micheli, F., Organtini, G., Rahatlou, S., Soffi, L., Brianza, L., Govoni, P., Martelli, A., Fatis, T. T. d., Monti, V., Pastrone, N., Trapani, P. P., Candelise, V., and Ricca, G. D.: 2015, *Nuclear Instruments and Methods in Physics Research A* **804**, 79

Belokurov, V., Evans, N. W., Moiseev, A., King, L. J., Hewett, P. C., Pettini, M., Wyrzykowski, L., McMahon, R. G., Smith, M. C., Gilmore, G., Sanchez, S. F., Udalski, A., Koposov, S., Zucker, D. B., and Walcher, C. J.: 2007, *ApJl* **671**, L9

Bian, F., Fan, X., McGreer, I., Cai, Z., and Jiang, L.: 2017, *ApJl* **837**, L12

Biretta, J. and Baggett, S.: 2013, *WFC3 Post-Flash Calibration*, Technical report

Borthakur, S., Heckman, T. M., Leitherer, C., and Overzier, R. A.: 2014, *Science* **346**, 216

Boutsia, K., Grazian, A., Giallongo, E., Fontana, A., Pentericci, L., Castellano, M.,

Zamorani, G., Mignoli, M., Vanzella, E., Fiore, F., Lilly, S. J., Gallozzi, S., Testa, V., Paris, D., and Santini, P.: 2011, *ApJ* **736**, 41

Bouwens, R. J., Illingworth, G. D., Oesch, P. A., Caruana, J., Holwerda, B., Smit, R., and Wilkins, S.: 2015a, *ArXiv e-prints*

Bouwens, R. J., Illingworth, G. D., Oesch, P. A., Trenti, M., Labbé, I., Bradley, L., Carollo, M., van Dokkum, P. G., Gonzalez, V., Holwerda, B., Franx, M., Spitler, L., Smit, R., and Magee, D.: 2015b, *ApJ* **803**, 34

Bouwens, R. J., Illingworth, G. D., Oesch, P. A., Trenti, M., Labbé, I., Franx, M., Stiavelli, M., Carollo, C. M., van Dokkum, P., and Magee, D.: 2012, *ApJl* **752**, L5

Bridge, C. R., Teplitz, H. I., Siana, B., Scarlata, C., Conselice, C. J., Ferguson, H. C., Brown, T. M., Salvato, M., Rudie, G. C., de Mello, D. F., Colbert, J., Gardner, J. P., Giavalisco, M., and Armus, L.: 2010, *ApJ* **720**, 465

Bruzual, G. and Charlot, S.: 2003, *MNRAS* **344**, 1000

Calzetti, D.: 1997, *The Astronomical Journal* **113**, 162

Casertano, S., de Mello, D., Dickinson, M., Ferguson, H. C., Fruchter, A. S., Gonzalez-Lopezlira, R. A., Heyer, I., Hook, R. N., Levay, Z., Lucas, R. A., Mack, J., Makidon, R. B., Mutchler, M., Smith, T. E., Stiavelli, M., Wiggs, M. S., and Williams, R. E.: 2000, *The Astronomical Journal* **120**, 2747

Conroy, C. and Kratter, K. M.: 2012, *ApJ* **755**, 123

Cowie, L. L., Barger, A. J., and Trouille, L.: 2009, *ApJ* **692**, 1476

de Barros, S., Vanzella, E., Amorín, R., Castellano, M., Siana, B., Grazian, A., Suh, H., Balestra, I., Vignali, C., Verhamme, A., Zamorani, G., Mignoli, M., Hasinger, G., Comastri, A., Pentericci, L., Pérez-Montero, E., Fontana, A., Giavalisco, M., and Gilli, R.: 2016, *Astronomy and Astrophysics* **585**, A51

Domínguez, A., Siana, B., Brooks, A. M., Christensen, C. R., Bruzual, G., Stark, D. P., and Alavi, A.: 2015, *MNRAS* **451**, 839

Dove, J. B., Shull, J. M., and Ferrara, A.: 2000, *ApJ* **531**, 846

Dye, S., Evans, N. W., Belokurov, V., Warren, S. J., and Hewett, P.: 2008, *MNRAS* **388**, 384

Eldridge, J. J. and Stanway, E. R.: 2009, *MNRAS* **400**, 1019

Erb, D. K.: 2015, *Nature* **523**, 169

Fan, X., Strauss, M. A., Becker, R. H., White, R. L., Gunn, J. E., Knapp, G. R., Richards, G. T., Schneider, D. P., Brinkmann, J., and Fukugita, M.: 2006, *The Astronomical Journal* **132**, 117

Fletcher, T. J., Robertson, B. E., Nakajima, K., Ellis, R. S., Stark, D. P., and Inoue, A.: 2018, *ArXiv e-prints*

Fujita, A., Martin, C. L., Mac Low, M.-M., and Abel, T.: 2003, *ApJ* **599**, 50

Fumagalli, M., O'Meara, J. M., and Prochaska, J. X.: 2011, *Science* **334**, 1245

Gnedin, N. Y., Kravtsov, A. V., and Chen, H.-W.: 2008, *ApJ* **672**, 765

Gonzaga, S., Hack, W., Fruchter, A., and Mack, J.: 2012, *The DrizzlePac Handbook. (Baltimore, STScI)*

Grimes, J. P., Heckman, T., Aloisi, A., Calzetti, D., Leitherer, C., Martin, C. L., Meurer, G., Sembach, K., and Strickland, D.: 2009, *ApJl Supp.* **181**, 272

Grimes, J. P., Heckman, T., Strickland, D., Dixon, W. V., Sembach, K., Overzier, R., Hoopes, C., Aloisi, A., and Ptak, A.: 2007, *ApJ* **668**, 891

Guaita, L., Pentericci, L., Grazian, A., Vanzella, E., Nonino, M., Giavalisco, M., Zamorani, G., Bongiorno, A., Cassata, P., Castellano, M., Garilli, B., Gawiser, E., Le Brun, V., Le Fevre, O., Lemaux, B. C., Maccagni, D., Merlin, E., Santini, P., Tasca, L. A. M., Thomas, R., Zucca, E., De Barros, S., Hathi, N. P., Amorin, R., Bardelli, S., and Fontana, A.: 2016, *ArXiv e-prints*

Heckman, T. M., Borthakur, S., Overzier, R., Kauffmann, G., Basu-Zych, A., Leitherer, C., Sembach, K., Martin, D. C., Rich, R. M., Schiminovich, D., and Seibert, M.: 2011, *ApJ* **730**, 5

Iwata, I., Inoue, A. K., Matsuda, Y., Furusawa, H., Hayashino, T., Kousai, K., Akiyama, M., Yamada, T., Burgarella, D., and Deharveng, J.-M.: 2009, *ApJ* **692**, 1287

Izotov, Y. I., Orlitova, I., Schaerer, D., Thuan, T. X., Verhamme, A., Guseva, N., and Worseck, G.: 2016, *ArXiv e-prints*

Izotov, Y. I., Schaerer, D., Worseck, G., Guseva, N. G., Thuan, T. X., Verhamme, A., Orlitová, I., and Fricke, K. J.: 2018, *MNRAS* **474**, 4514

Janknecht, E., Reimers, D., Lopez, S., and Tytler, D.: 2006, *Astronomy and Astrophysics* **458**, 427

Jones, T., Ellis, R. S., Richard, J., and Jullo, E.: 2013a, *ApJ* **765**, 48

Jones, T. A., Ellis, R. S., Schenker, M. A., and Stark, D. P.: 2013b, *ApJ* **779**, 52

Law, D. R., Steidel, C. C., Erb, D. K., Larkin, J. E., Pettini, M., Shapley, A. E., and Wright, S. A.: 2007, *ApJ* **669**, 929

Leitet, E., Bergvall, N., Hayes, M., Linné, S., and Zackrisson, E.: 2013, *Astronomy and Astrophysics* **553**, A106

Leitet, E., Bergvall, N., Piskunov, N., and Andersson, B.-G.: 2011, *Astronomy and Astrophysics* **532**, A107

Leitherer, C., Ferguson, H. C., Heckman, T. M., and Lowenthal, J. D.: 1995, *ApJl* **454**, L19

Leitherer, C., Schaerer, D., Goldader, J. D., Delgado, R. M. G., Robert, C., Kune, D. F., de Mello, D. F., Devost, D., and Heckman, T. M.: 1999, *ApJl Supp.* **123**, 3

Ma, X., Kasen, D., Hopkins, P. F., Faucher-Giguere, C.-A., Quataert, E., Keres, D., and Murray, N.: 2015, *ArXiv e-prints*

MacKenty, J. and Smith, L.: 2012, *WFC3 SMOV Proposal 11450: The Photometric Performance and Calibration of WFC3/UVIS*, Technical report

Mostardi, R. E., Shapley, A. E., Nestor, D. B., Steidel, C. C., Reddy, N. A., and Trainor, R. F.: 2013, *ApJ* **779**, 65

Mostardi, R. E., Shapley, A. E., Steidel, C. C., Trainor, R. F., Reddy, N. A., and Siana, B.: 2015, *ArXiv e-prints*

Nestor, D. B., Shapley, A. E., Kornei, K. A., Steidel, C. C., and Siana, B.: 2013, *ApJ* **765**, 47

Nestor, D. B., Shapley, A. E., Steidel, C. C., and Siana, B.: 2011, *ApJ* **736**, 18

Nonino, M., Dickinson, M., Rosati, P., Grazian, A., Reddy, N., Cristiani, S., Giavalisco, M., Kuntschner, H., Vanzella, E., Daddi, E., Fosbury, R. A. E., and Cesarsky, C.: 2009, *ApJl Supp.* **183**, 244

Oesch, P. A., Bouwens, R. J., Illingworth, G. D., Labbé, I., Franx, M., van Dokkum, P. G., Trenti, M., Stiavelli, M., Gonzalez, V., and Magee, D.: 2013, *ApJ* **773**, 75

O'Meara, J. M., Prochaska, J. X., Worseck, G., Chen, H.-W., and Madau, P.: 2013, *ApJ* **765**, 137

Prochaska, J. X., Worseck, G., and O'Meara, J. M.: 2009, *ApJl* **705**, L113

Quider, A. M., Pettini, M., Shapley, A. E., and Steidel, C. C.: 2009, *MNRAS* **398**, 1263

Rafelski, M., Teplitz, H. I., Gardner, J. P., Coe, D., Bond, N. A., Koekemoer, A. M., Gro-

gin, N., Kurczynski, P., McGrath, E. J., Bourque, M., Atek, H., Brown, T. M., Colbert, J. W., Codoreanu, A., Ferguson, H. C., Finkelstein, S. L., Gawiser, E., Giavalisco, M., Gronwall, C., Hanish, D. J., Lee, K.-S., Mehta, V., de Mello, D. F., Ravindranath, S., Ryan, R. E., Scarlata, C., Siana, B., Soto, E., and Voyer, E. N.: 2015, *The Astronomical Journal* **150**, 31

Rao, S. M., Turnshek, D. A., and Nestor, D. B.: 2006, *ApJ* **636**, 610

Ribaudo, J., Lehner, N., and Howk, J. C.: 2011, *ApJ* **736**, 42

Robertson, B. E., Ellis, R. S., Furlanetto, S. R., and Dunlop, J. S.: 2015, *ApJl* **802**, L19

Robertson, B. E., Furlanetto, S. R., Schneider, E., Charlot, S., Ellis, R. S., Stark, D. P., McLure, R. J., Dunlop, J. S., Koekemoer, A., Schenker, M. A., Ouchi, M., Ono, Y., Curtis-Lake, E., Rogers, A. B., Bowler, R. A. A., and Cirasuolo, M.: 2013, *ApJ* **768**, 71

Rudie, G. C., Steidel, C. C., Shapley, A. E., and Pettini, M.: 2013, *ApJ* **769**, 146

Schlafly, E. F. and Finkbeiner, D. P.: 2011, *ApJ* **737**, 103

Shapley, A. E., Steidel, C. C., Pettini, M., and Adelberger, K. L.: 2003, *ApJ* **588**, 65

Shapley, A. E., Steidel, C. C., Strom, A. L., Bogosavljević, M., Reddy, N. A., Siana, B., Mostardi, R. E., and Rudie, G. C.: 2016, *ApJl* **826**, L24

Siana, B., Shapley, A. E., Kulas, K. R., Nestor, D. B., Steidel, C. C., Teplitz, H. I., Alavi, A., Brown, T. M., Conselice, C. J., Ferguson, H. C., Dickinson, M., Giavalisco, M., Colbert, J. W., Bridge, C. R., Gardner, J. P., and de Mello, D. F.: 2015, *ApJ* **804**, 17

Siana, B., Teplitz, H. I., Colbert, J., Ferguson, H. C., Dickinson, M., Brown, T. M., Conselice, C. J., de Mello, D. F., Gardner, J. P., Giavalisco, M., and Menanteau, F.: 2007, *ApJ* **668**, 62

Siana, B., Teplitz, H. I., Ferguson, H. C., Brown, T. M., Giavalisco, M., Dickinson, M., Chary, R.-R., de Mello, D. F., Conselice, C. J., Bridge, C. R., Gardner, J. P., Colbert, J. W., and Scarlata, C.: 2010, *ApJ* **723**, 241

Steidel, C. C., Adelberger, K. L., Shapley, A. E., Pettini, M., Dickinson, M., and Giavalisco, M.: 2003, *ApJ* **592**, 728

Steidel, C. C., Pettini, M., and Adelberger, K. L.: 2001, *ApJ* **546**, 665

Teplitz, H. I., Rafelski, M., Kurczynski, P., Bond, N. A., Grogin, N., Koekemoer, A. M., Atek, H., Brown, T. M., Coe, D., Colbert, J. W., Ferguson, H. C., Finkelstein, S. L., Gardner, J. P., Gawiser, E., Giavalisco, M., Gronwall, C., Hanish, D. J., Lee, K.-S., de

Mello, D. F., Ravindranath, S., Ryan, R. E., Siana, B. D., Scarlata, C., Soto, E., Voyer, E. N., and Wolfe, A. M.: 2013, *The Astronomical Journal* **146**, 159

Vanzella, E., de Barros, S., Castellano, M., Grazian, A., Inoue, A. K., Schaerer, D., Guaita, L., Zamorani, G., Giavalisco, M., Siana, B., Pentericci, L., Giallongo, E., Fontana, A., and Vignali, C.: 2015, *Astronomy and Astrophysics* **576**, A116

Vanzella, E., de Barros, S., Vasei, K., Alavi, A., Giavalisco, M., Siana, B., Grazian, A., Hasinger, G., Suh, H., Cappelluti, N., Vito, F., Amorin, R., Balestra, I., Brusa, M., Calura, F., Castellano, M., Comastri, A., Fontana, A., Gilli, R., Mignoli, M., Pentericci, L., Vignali, C., and Zamorani, G.: 2016, *ApJ* **825**, 41

Vanzella, E., Giavalisco, M., Inoue, A. K., Nonino, M., Fontanot, F., Cristiani, S., Grazian, A., Dickinson, M., Stern, D., Tozzi, P., Giallongo, E., Ferguson, H., Spinrad, H., Boutsia, K., Fontana, A., Rosati, P., and Pentericci, L.: 2010, *ApJ* **725**, 1011

Vanzella, E., Guo, Y., Giavalisco, M., Grazian, A., Castellano, M., Cristiani, S., Dickinson, M., Fontana, A., Nonino, M., Giallongo, E., Pentericci, L., Galametz, A., Faber, S. M., Ferguson, H. C., Grogin, N. A., Koekemoer, A. M., Newman, J., and Siana, B. D.: 2012, *ApJ* **751**, 70

Vasei, K., Siana, B., Shapley, A. E., Quider, A. M., Alavi, A., Rafelski, M., Steidel, C. C., Pettini, M., and Lewis, G. F.: 2016, *ApJ* **831**, 38

Appendix

A1 Converting Covering Fraction to Escape Fraction

There are a number of definitions of the LyC escape fraction in the literature, “relative escape fraction”, “absolute escape fraction”, “dust free escape fraction”, etc.. This has lead to some confusion about how they are related to the physical covering fraction or the depth of the low-ionizing absorption lines. To avoid this confusion, we derive here what exactly each of these terms represents for three simplified scenarios of dust distribution within a patchy ISM. These simplified cases are a) a dust free model; b) a uniform screen of dust and c) dust only located in dense clouds. Cartoons of these models are shown in Figure 3.13 where dusty regions are shown as solid black dots. We note that the precise location of the uniform dust screen in model (b) does not affect the calculations below.

We also note that the covering fraction inferred by the depth of the absorption (denoted here by $C_{F'}$) is not necessarily the same as the physical covering fraction of the dense clouds (C_F). Observationally, we can only measure $C_{F'}$ which is defined as the ratio of the observed flux density at the wavelength of the absorption line (assumed to be completely saturated in the dense clouds), to the observed continuum flux density (at around 1500Å): $1 - C_{F'} = \frac{F_{line,obs}}{Fcont,obs}$. Therefore, we report our escape fractions as a function of $C_{F'}$:

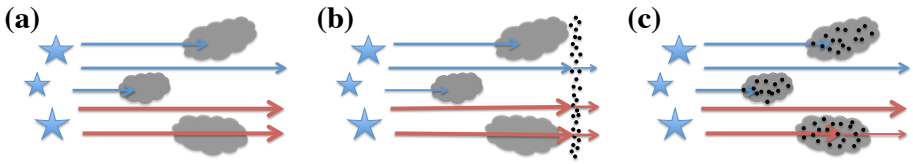

Figure 3.13: The three simple models for the distribution of dust within a patchy ISM/CGM arm depicted: (a) no dust; (b) a uniform dust screen, (c) dust only within the gas clumps. The ionizing and non-ionizing fluxes are represented by blue and red arrows, respectively.

A1.1 Case (a) No dust :

For the dust free case, the LyC flux density and the flux density in the absorption lines get completely absorbed by the clouds while the 1500 Å continuum flux density remains unaffected by the gas clouds:

$$F_{LyC,out} = F_{LyC,stel} \times (1 - C_F); F_{1500,out} = F_{1500,stel} \tag{3.4}$$

$$1 - C_{F'} = \frac{F_{line,obs}}{F_{cont,obs}} = \frac{F_{1500,stel} \times (1 - C_F)}{F_{1500,stel}} = 1 - C_F \tag{3.5}$$

So here $C_F = C_{F'}$, which results in:

$$f_{esc,rel} = \frac{\left(F_{LyC}/F_{1500}\right)_{out}}{\left(F_{LyC}/F_{1500}\right)_{stel}} = 1 - C_F = 1 - C_{F'} \tag{3.6}$$

$$f_{esc,abs} = \frac{F_{LyC,out}}{F_{LyC,stel}} = 1 - C_F = 1 - C_{F'} \tag{3.7}$$

In this case, $f_{esc,rel}$ and $f_{esc,abs}$ are the same. In the literature, this is sometimes referred to as the dust free escape fraction.

A1.2 Case (b) Screening dust :

In this case we add a layer of uniform dust to the previous geometry. So all the flux densities are now the dust attenuated fluxes of the previous case:

$$F_{LyC,out} = F_{LyC,stel} \times (1 - C_F) \times e^{-\tau_{dust,LyC}}; F_{1500,out} = F_{1500,stel} \times e^{-\tau_{dust,LyC}} \tag{3.8}$$

$$1 - C_{F'} = \frac{F_{line,obs}}{F_{cont,obs}} = \frac{F_{1500,stel} \times (1 - C_F)}{F_{1500,stel}} = 1 - C_F \tag{3.9}$$

Again in this geometry we have $C_F = C_{F'}$, which results in:

$$f_{esc,rel} = \frac{\left(F_{LyC}/F_{1500}\right)_{out}}{\left(F_{LyC}/F_{1500}\right)_{stel}} = 1 - C_{F'} \times e^{-(\tau_{dust,LyC} - \tau_{dust,1500})} \tag{3.10}$$

$$f_{esc,abs} = \frac{F_{LyC,out}}{F_{LyC,stel}} = 1 - C_{F'} \times e^{-\tau_{dust,LyC}} \tag{3.11}$$

Here neither $f_{esc,rel}$ nor $f_{esc,abs}$ are not equivalent to the $1 - C_{F'}$.

A1.3 Case (c) Dust in clouds:

In this case the dust closely traces the dense gas. We believe that this is the model that most closely resembles reality, as any significant dust will be accompanied by opaque columns of gas (both in the LyC and the interstellar absorption lines, Gnedin et al., 2008). Though the dust has practically no effect on the line or LyC flux (they get absorbed predominantly by the gas), it attenuates the observed continuum flux. So we have:

$$F_{LyC,out} = F_{LyC,stel} \times (1 - C_F); F_{1500,out} = F_{1500,stel} \times (1 - C_F + C_F \times e^{-\tau_{dust,1500}}) \quad (3.12)$$

$$1 - C_{F'} = \frac{F_{line,obs}}{F_{cont,obs}} = \frac{F_{1500,stel} \times (1 - C_F)}{F_{1500,stel} \times (1 - C_F + C_F \times e^{-\tau_{dust,1500}})} \neq 1 - C_F \quad (3.13)$$

Interestingly, in such a scenario the covering fraction based on the depth of the low ionization absorption lines is actually different from the physical covering fraction, i.e. $C_F \neq C_{F'}$. As such we end up with the following relations for the escape fractions:

$$f_{esc,rel} = \frac{\left(F_{LyC}/F_{1500}\right)_{out}}{\left(F_{LyC}/F_{1500}\right)_{stel}} = 1 - C_{F'} \quad (3.14)$$

$$f_{esc,abs} = \frac{F_{LyC,out}}{F_{LyC,stel}} = 1 - C_F = 1 - \frac{C_{F'}}{C_{F'} + (1 - C_{F'}) \times e^{-\tau_{dust,1500}}} \quad (3.15)$$

Therefore, $f_{esc,rel}$ is, in fact, equal to the ratio of the observed flux density in the line to the observed continuum flux density, $f_{esc,rel} = 1 - C_{F'}$. Since $1 - C_{F'}$ is a common observable, it is best to compare this measurement to that of $f_{esc,rel}$ as we have done in this work.